



Changes in future precipitation mean and variability across scales

Kevin Schwarzwald

Center for Robust Decision-Making on Climate and Energy Policy (RDCEP)

Andrew Poppick

Dept. of Mathematics and Statistics, Carleton College

Maria Rugenstein

Max Planck Institute for Meteorology, Hamburg

Jonah Bloch-Johnson

National Centre for Atmospheric Science, University of Reading

Jiali Wang

Environmental Science Division, Argonne National Laboratory

David McInerney

Dept. of Civil and Env. Engineering, Univ. of Adelaide

Elisabeth J. Moyer*

Center for Robust Decision-Making on Climate and Energy Policy (RDCEP)

**Corresponding author address:* Dept. of the Geophysical Sciences, Univ. of Chicago, 5374 S Ellis Ave, Chicago, IL, USA.

E-mail: moyer@uchicago.edu

ABSTRACT

Changes in precipitation variability can have large societal consequences, whether at the short timescales of flash floods or the longer timescales of multi-year droughts. Recent studies have suggested that in future climate projections, precipitation variability rises more steeply than does its mean, leading to concerns about societal impacts. This work evaluates changes in mean precipitation over a broad range of spatial and temporal scales using a range of models from high-resolution regional simulations to millennial-scale global simulations. Results show that changes depend on the scale of aggregation and involve strong regional differences. On local scales that resolve individual rainfall events (hours and tens of kilometers), changes in precipitation distributions are complex and variances rise substantially more than means, as is required given the well-known disproportionate rise in precipitation intensity. On scales that aggregate across many events, distributional changes become simpler and variability changes smaller. At regional scale, future precipitation distributions can be largely reproduced by a simple transformation of present-day precipitation involving a multiplicative shift and a small additive term. The “extra” broadening is negatively correlated with changes in mean precipitation: in strongly “wetting” areas, distributions broaden less than expected from a simple multiplicative mean change; in “drying” areas, distributions narrow less. Precipitation variability changes are therefore of especial concern in the subtropics, which tend to dry under climate change. Outside the tropics, variability changes are similar on timescales from days to decades, i.e. show little frequency dependence. This behavior is highly robust across models, suggesting it may stem from some fundamental constraint.

1. Introduction

Changes in climate variability may be as important for societal impacts as are changes in climate means, and potential increases in precipitation variability are of particular concern for human welfare. Precipitation variability matters for societal risks and impacts on all timescales: months or longer for droughts affecting crop yields, weeks for large-scale flooding, and hours or shorter for severe storms that produce field-level crop damage or loss of life. Studies suggest that increases in interannual precipitation variability may impact food security by altering streamflow (Abghari et al. 2013), snowpack (Hamlet et al. 2005; Gornall et al. 2010), drought incidence Barlow et al. (2001), and crop yields (Riha et al. 1996), while many extreme weather events are driven by short-timescale patterns (Vitart et al. 2012). On all timescales, variability changes are especially important for threshold-defined extremes, whose frequency is more sensitive to changes in the variability of a distribution than its mean (Katz and Brown 1992).

Given its importance to human impacts, an increasing number of studies have examined precipitation variability in models and historical data. Studies robustly suggest that precipitation variability will increase in future warmer, wetter climate conditions (e.g. Meehl et al. 1994; Liang et al. 1995; Zwiers and Kharin 1998; Räisänen 2002; Wetherald 2010; Lu and Fu 2010; Pendergrass et al. 2017; He and Li 2018). Increased future variability is not surprising and would result even in the simplest conceptual model of precipitation changes: if climate change has a multiplicative effect on precipitation, its distribution broadens following the change in the mean. However, while early studies argued that changes in precipitation variability should follow mean changes (e.g Rind et al. 1988; Groisman et al. 1999), most recent studies have concluded that variability changes actually exceed those in means, in all but the highest latitudes (e.g. Räisänen 2002; Lu and Fu 2010; Pendergrass et al. 2017; He and Li 2018).

Comparison of results across studies is complicated by the fact that different studies use different metrics of variability, and few have systematically addressed the comparisons across spatial and temporal scales. The most commonly used definition of “variability” is the variance or standard deviation of a precipitation timeseries, often calculated after removing a long-term and/or seasonal trend (e.g. Räisänen 2002; Lu and Fu 2010; Brown et al. 2017; Pendergrass et al. 2017; He and Li 2018). Some studies use instead the inter-quartile range (IQR), which is not affected by the behavior of the extreme tails (e.g. Mearns et al. 1995). Early studies characterize variability in terms of parameters derived from fitting gamma distributions to daily precipitation intensity (e.g. Semenov and Bengtsson 2002; Groisman et al. 1999). (An invariant shape parameter suggests that variability changes follow a mean change.)

Studies also differ widely in the spatial and temporal scales over which precipitation is aggregated. Spatial scales considered range from individual raingauge measurements (e.g. Groisman et al. 1999) to sub-continental or even global precipitation (e.g. Kripalani et al. 2007), and temporal aggregations from 3 hours to 1 year or more. The degree of aggregation appears to affect conclusions. For example, Hunt and Elliott (2004) show that precipitation distributions shift differently relative to the mean with increasing spatial aggregation, and Sun et al. (2012) suggest that changes in local precipitation may differ across timescales. On the other hand, Pendergrass et al. (2017) find no differences in the behavior of highly spatially aggregated precipitation (global or global land) at timescales from daily to 3 years, and Brown et al. (2017) find similar results at daily to decadal timescales for the Asian Monsoon area.

Modeling studies do come to some robust conclusions. All agree that locally, the sign of variability change largely follows the sign of the mean or median change (e.g. Rind et al. (1988) in a GCM, or Mearns et al. (1995) in a regional climate model), though the correlation may vary regionally. Multiple studies with modern-era GCMs have found that when precipitation is spa-

tially aggregated over large regions, the magnitude of variability change generally exceeds that of mean change, regardless of timescale: e.g. for interannual variability, in east Asia (Lu and Fu 2010), south Asia (Kripalani et al. 2007), climatological ascending regions (He and Li 2018), and for both interannual and sub-annual variability, at all but high-latitudes land (Pendergrass et al. (2017), who find changes of $\sim 3\text{-}4\%/K$ in global mean variability and $\sim 4\text{-}5\%/K$ for the global land mean while citing mean changes of $\sim 2\%/K$). At higher latitudes, variability change is found to largely equal mean change, in GCMs (Hennessy et al. 1997; Pendergrass et al. 2017) and idealized climate models (O’Gorman and Schneider 2009), with some supporting evidence from local observations (Groisman et al. 1999).

The physical drivers that underlie these effects are not well understood. Zeroeth order physics does suggest that precipitation variability should increase more than the mean on the small temporal and spatial scales of individual precipitation events (hours and 10s of km, when precipitation timeseries would show frequent zeroes). It is well understood that under climate change, the intensity of precipitation rises more steeply than does total precipitation, since intensity roughly follows the Clausius-Clapeyron relationship ($\sim 6\text{-}7\%/K$) while total rainfall increases by only $1\text{-}2\%/K$ in transient simulations (e.g. Hennessy et al. (1997); Allen and Ingram (2002) (See also Pendergrass and Hartmann (2014); Pendergrass and Knutti (2018).) The dry intervals between rainfall occurrences must then increase. The effect implies some change in the characteristics of precipitation events, which could involve reductions in their duration, frequency, size, or any combination of these (Trenberth et al. 2003; Sun et al. 2007; Chang et al. 2016; Wasko et al. 2016; Dai et al. 2017; Chen et al. 2020). Regardless of the cause, an increase in dry intervals necessarily means an amplification of measured variability over that driven by a simple multiplicative mean change.

On aggregation scales that integrate over multiple events, the relevant physics is less clear. Both O’Gorman and Schneider (2009) and He and Li (2018) suggest that changes in precipitation vari-

ability in ascending regions may be driven by changes in updraft velocities (even at inter-annual timescales, in the latter study), allowing changes in precipitation rates above or below that otherwise allowed by energetics. In descending regions, He and Li (2018) posit that moisture availability is too low for these changes to matter, so that precipitation variability should rise as the mean. The drivers of the apparent increases seen in model studies remain an open question.

In this work, we seek to extend on previous studies by conducting self-consistent or near-consistent studies of precipitation changes across a wider range of spatial and temporal scales: from 3-hourly to decadal in timescale and from 12 km to global in spatial scale. Full consistency is not possible since the highest-resolution, finest-temporal scale analyses require simulations too computationally expensive to be extended for many decades. However, we can obtain overlapping analyses by using a combination of dynamically downscaled regional simulations, centennial-scale global simulations, and a new ensemble of millennial-scale, equilibrated global model runs from the Long Run Model Intercomparison Project (LongRunMIP, Rugenstein et al. (2019)). The goal is to obtain a systematic understanding of the relationship between mean and variability changes across scales and across space, to answer the questions: how and where do changes in precipitation variability deviate from those in the mean?

The remainder of this paper is laid out as follows. After introducing data sources in Section 2 and methods in Section 3, we address scientific issues in three broad parts. First, in Section 4, we examine how precipitation distributions (and their future changes) alter when aggregated across space or time. As expected, distributional changes are complex at the hyperlocal scale of individual precipitation events, but simplify and become smaller with aggregation. Scale-dependent behavior largely ceases beyond spatial scales of a few hundred km or temporal scales of a month. Second, in Section 5, we consider precipitation aggregated beyond these scales and examine how distributions change in warmer climate conditions. We show that distributional transformations resemble simple

multiplicative and additive shifts. Finally, in Section 6, we restrict our analysis to one aspect of a precipitation distribution, its standard deviation; any “extra” variability then appears as a standard deviation whose change is larger than that in the mean. We evaluate the geographic distribution of variability changes, and find that while changes in precipitation variability broadly scale with those in means, they include a small “extra” variability component that is negatively correlated with mean changes. This behavior is robust across models and across frequency bands.

2. Data sources

We use three different types of climate model simulations, totaling 19 pairs of present and future runs, to cover a large range of temporal and spatial resolution (Table 1).

Short timescales. To examine precipitation changes at the smallest spatial and temporal timescales, which resolve individual precipitation events, we use 3-hourly precipitation from regional rather than global model output. We use 12×12 km dynamically downscaled regional simulations over the continental U.S. made with the Weather Research & Forecasting model (WRF, Skamarock et al. (2008)) driven by historical and RCP8.5 (Representative Concentration Pathway 8.5 W/m^2 van Vuuren et al. 2011) simulations from CCSM4 (Wang and Kotamarthi 2015; Chang et al. 2016). Because of computational demands, high-resolution runs are only 10 years long (1995-2004 for a ‘baseline’ and 2085-2094 for an RCP8.5 ‘future’ run). Runs are spectrally nudged at the 1200 km wavelength, but no bias correction is applied. (Our results are robust to the use of nudging.) These runs allow us to evaluate precipitation behavior at the hyperlocal level, but can also be aggregated to monthly precipitation at near-continental scale. While the use of a single model makes our high-resolution analysis more limited than that allowed by the multi-model CMIP5 and LongRunMIP ensembles, WRF output is useful for qualitatively illustrating changes in precipitation behavior on aggregation at high resolution.

Medium timescales. Following prior studies of precipitation variability, we analyze daily and monthly precipitation in model output from the CMIP5 (Coupled Model Intercomparison Project phase 5) archive (Taylor et al. 2011). Rather than construct a multi-model mean, we analyze 12 of the 28 CMIP5 models individually, choosing models with climate sensitivities representative of the ensemble and that are reasonably independent. That is, we avoid models that share multiple components or code, informed by the climate model ‘genealogy’ developed by Knutti et al. (2013). The selected models have different resolutions (from 0.94° to 2.79°) and different representations of atmospheric and oceanic processes, but were run with the same forcing scenario. For each model, we evaluate changes between the last 30 years of a pre-industrial control simulation and the last 30 years (2070-2099) of the business-as-usual RCP8.5 forcing scenario. Models have 365-day calendars, so leap days do not factor in the analysis. While some models provide multiple realizations, we use only one per model.

Long timescales. The CMIP5 ensemble is not well-suited for examining changes in low-frequency variability, since runs are both non-stationary and relatively short: most models archive only ~ 100 years of future forcing experiments. Many climatological phenomena of socioeconomic interest occur on interannual timescales, including El Niño/Southern Oscillation (ENSO), and multi-year droughts, whose potential increase is a concern. To resolve variability changes at low frequencies, we use monthly precipitation from millennial-scale, near-equilibrated (stationary) output from 6 models from the Long-Run Model Intercomparison Project (LongRunMIP, Rugenstein et al. (2019)), with models chosen for having at least 1000 years of data from both control and forced scenarios. Models studied are often from the same modeling groups as those of CMIP5 but in some cases are run at coarser resolution. We use primarily the forcing scenario of abrupt quadrupling of CO_2 , but for the CCSM3 model also include a near-quintupling scenario (abrupt rise from 289

to 1400 ppm). To ensure the climate system has equilibrated, we use the last 500 years of both control and forced runs.

Model suitability. Studies of precipitation changes in models must always confront the limitations of the models themselves. Several known issues should affect model variability on spatial and time scales that resolve individual events, which are addressed in this work in Figure 1. General circulation models have well-known biases toward excess light precipitation resulting in too few dry periods (e.g. Sun et al. 2006), and difficulty capturing the timing and magnitude of the diurnal cycle (e.g. Covey et al. 2016). Trenberth et al. (2017) show that on 3-hourly timescales, the CESM model produces too-low precipitation variability, especially in the tropics and monsoon regions where standard deviations can be half of observed values. Model biases in precipitation organization are reduced but not eliminated in high-resolution simulations (e.g. Chang et al. (2016, 2018), who evaluate the same WRF runs used here). Global climate model runs also have too low a spatial resolution to resolve hurricanes and tropical cyclones (Emanuel 2013), which are estimated to contribute 3.3% of low-latitudes rainfall (between 35N–35S) (Yokoyama and Takayabu 2008).

When precipitation is aggregated beyond the event scale (i.e. timeseries have few zeroes), as in the bulk of this study, models have been shown to perform reasonably well in several contexts. For example, Dai (2006) show that CMIP3 models can reasonably simulate the partitioning of variability by seasonal to interannual timescales, other than in the tropical Pacific. However, in a regional study, Rupp et al. (2013) showed that variability in monthly precipitation in CMIP5 models is generally too low in the Pacific Northwest.

Assessments of precipitation variability on longer, interannual timescales are mixed. Regional studies suggest that some major phenomena are reasonably well reproduced: for example, the relationship between ENSO and the Pacific Decadal Oscillation (PDO) (Fuentes-Franco et al. 2016) and PDO teleconnections (Polade et al. 2013). Others phenomena remain problematic: ENSO

in particular may be poorly represented, especially in older models (e.g. Bellenger et al. 2014) and the North Atlantic Oscillation may have regional biases (Davini and Cagnazzo 2014)). On still longer timescales (decadal or longer), the lack of a long observational record makes evaluating model performance difficult, but several studies suggest that precipitation variability may be underestimated (Ault et al. 2012; Cheung et al. 2017; Biasutti 2013). Despite these limitations, we note that models may be informative about changes even given biases. Conversely, successful modeling of historical climates by models does not itself guarantee accuracy in future projections (e.g. Eyring et al. 2019).

3. Methods

Analysis in this work falls into two broad categories. In Sections 4 and 5, we analyze shifts in the distribution of precipitation at different temporal and spatial aggregation levels, using quantile-quantile and quantile ratio plots. In Sections 4 and 6, we examine the relationships between changes in precipitation variability and means. For this purpose, we define variability as the standard deviation of a timeseries after the seasonal cycle and any long-term trend are removed. We determine the relationship between precipitation mean and variability changes across space using orthogonal least squares regression. In some cases, to isolate variability at different timescales, we first use spectral density analysis to determine the integrated variability in particular frequency bands. These methods are described in detail below and in Supplementary Online Material. Throughout the work, we adopt as a starting point that a fractional change in mean precipitation should produce the same fractional change in variability ($\mu_f/\mu_i = \sigma_f/\sigma_i$, where the subscripts f and i denote the future and present or “initial” conditions), and consider in what circumstances and to what extent the actual changes deviate from this expectation. That precipitation distributions differ by a multiplicative shift to first order is a common assumption in bias-correction studies

(e.g. Ines and Hansen (2006) or Goyal et al. (2012)), and a starting point in previous precipitation variability studies (e.g. Pendergrass et al. (2017)). To quantify these deviations, we use the change in the coefficient of variation $\varepsilon_{\sigma} = (\sigma_f/\mu_f) / (\sigma_i/\mu_i)$, the ‘additional’ realized precipitation variability change beyond that expected based on the mean change. If $\varepsilon_{\sigma} = 1$, then the variability change equals that in mean; if $\varepsilon_{\sigma} > 1$, the variability change exceeds that in mean, and vice-versa.

a. Data processing: detrending and deseasonalizing

In many analyses here we both detrend and deseasonalize the data. In the WRF and CMIP5 runs, forcing is evolving and climate is non-stationary over the 10- or 30-year timeseries used as the future climate state. Removing long-term trends avoids spurious broadening of precipitation distributions and spurious signals in spectral analysis. We detrend by subtracting a linear fit for precipitation in each model grid cell. We deseasonalize because we treat seasonal variability as part of the mean climate state. Deseasonalization is done separately for pre-industrial control and future runs, so evolving seasonality across time blocks is not included in estimated changes in precipitation variability (although any changes in seasonality *within* each time period are included). Daily data are deseasonalized by removing 12 harmonics, and monthly data by subtracting the monthly mean for each timeseries. For daily data, we believe that 12 harmonics is a reasonable compromise between complexity and smoothness; note that removing the daily average would be equivalent to removing 182 harmonics. (See Supplementary Online Material Section S1.1 for more discussion and comparison of deseasonalizing methods.) Note that a seasonal cycle in variability may remain even after the mean seasonal cycle is removed. We therefore include analyses by season (winter and summer) in some cases to verify that our results are not seasonally dependent. Figures here should be assumed to involve detrended and deseasonalized data unless specified otherwise.

b. Evaluating shifts in distributions

We examine changes in the shapes of entire distributions by determining how individual quantiles change under future climate conditions. A quantile is a measure of a distribution associated with a specified probability, such that the proportion of the distribution below the quantile value corresponds to that probability. (For example, the value of the 0.5 quantile is the median.) The quantile-quantile (“q-q”) plots of Sections 4 and 5 compare equivalent precipitation quantiles in present and future climate simulations. If the two distributions are equal, the q-q plot lies on the line $y = x$; if the transformation is a simple multiplicative scaling, the q-q plot is a line whose slope is the fractional mean shift μ_f/μ_i . If the transformation also includes additive changes, producing a change ε_σ in the coefficient of variation, the q-q plot will have a non-zero intercept and slope equal to $\varepsilon_\sigma \cdot \mu_f/\mu_i = \sigma_f/\sigma_i$. A curved q-q plot implies that the distributions cannot be related by only additive and multiplicative changes. Quantile ratio plots provide a different representation of the same information, with the ratio of the present and future quantiles plotted against the cumulative probability.

We include all data points inclusive of periods of zero precipitation. For the quantile ratio plots, we begin the x axis at the first non-zero quantile in the denominator. For 3-hourly precipitation in 10-year WRF runs, the number of quantiles is 29,200; for daily precipitation in 30-year CMIP5 timeseries it is 10,950; for monthly precipitation in 500-year LongRunMIP timeseries it is 6,000.

We compare future precipitation distributions to two synthetic distributions constructed by simple transformations of present-day model precipitation. The first transformation is a simple multiplicative shift, i.e. we multiply all quantiles of the present-day distribution X_i by the fractional mean change:

$$X'_f = X_i \cdot (\mu_f/\mu_i) \quad (1)$$

The quantile ratio plot is then a horizontal line of value $y = (\mu_f/\mu_i)$. This transformation results in equal changes in the mean and variability of the precipitation distribution.

The second transformation combines a multiplicative shift with an additive change so that the mean and variability changes need not be equal:

$$\begin{aligned} X_f'' &= (X_i - \mu_i) \cdot \sigma_f/\sigma_i + \mu_f \\ &= X_i \cdot (\mu_f/\mu_i) \cdot \varepsilon_\sigma + \mu_f(1 - \varepsilon_\sigma). \end{aligned} \quad (2)$$

The quantile ratio plot is then non-linear; see Section S1.3 for a detailed discussion. The second transformation combines an additive and a multiplicative change, adding a correction to the first transformation to account for a widening or narrowing of the distribution beyond the mean shift. To test how well these transformations reproduce future distributions, we apply a two-sample Anderson-Darling test. See Supplementary Online Material section S1.2 for details.

This transformation is not equivalent to that of Pendergrass and Hartmann (2014), who also characterize shifts in distributions using a two-component model. The effects of their ‘shift’ and ‘increase’ modes depend on the underlying event distribution, and generally will not be equal to multiplicative and additive changes. The ‘shift’ mode would affect variability only on aggregation timescales shorter than the monthly precipitation used in most analyses here.

c. Spectral analysis

In Section 6, we use spectral density analysis to decompose timeseries of precipitation variability into frequency components. For each deseasonalized and detrended timeseries, we calculate a power spectrum as the squared absolute value of the discrete Fourier transform, integrate the spectrum over the frequencies of interest, and take the square root to obtain the “integrated variability” as in Klavans et al. (2016). The method effectively determines that portion of the total precipi-

tation variability associated with a particular frequency band. Integrated variability is reported in units of precipitation per time, e.g. cm/month or kg/m²/s. We characterize variability changes by taking the ratio of integrated variabilities between present and future simulations.

d. Orthogonal least squares regression

After calculating changes in precipitation means and integrated variability at each grid cell, we characterize their relationship using orthogonal regression instead of ordinary least squares regression. Orthogonal regression minimizes the sum of the orthogonal distances between each point and the regression line, and is appropriate when an equal amount of noise is present in both variables, as may be reasonable to assume in this setting. By contrast, the ordinary least-squares fit minimizes the distance between data points and regression line in only one dimension, implicitly assuming that there is no noise in the independent variable. As a result, the ordinary least-squares fit will underestimate the slope of the underlying relationship, a phenomenon known as “regression dilation.” (See e.g. Frost and Thompson (2000).) In a two-dimensional orthogonal regression, the slope of the best-fit line is equivalent to the slope of the first principal component of the data (the eigenvector with the highest eigenvalue). Because we are interested in fractional changes, we take the log of variability and mean changes before fitting.

e. Uncertainty quantification

It is important to assess uncertainty in any changes estimated from limited data. In analyses here, uncertainties can be large when model timeseries are short relative to the scales of interest: for example, we consider interannual variability in 30-year segments of CMIP5 runs. We characterize uncertainties using a moving-block permutation test. We construct two synthetic runs by randomly drawing 5-year blocks without replacement from a pool of both the control and future

runs; calculate the change in the variable of interest, using the methodology above; repeat for 1,000 draws to construct a distribution of results; then compare to the actual estimated change and calculate a p-value. All blocks start on Jan. 1. The p-value is the proportion of estimated changes from the synthetic runs that are larger in magnitude than the actual change: a small p-value would imply that the data show evidence of a nonzero change. In figures here we use 0.05 as our significance cutoff. Large p-values may arise either because the true change is small in an absolute sense or because the statistical uncertainty is large.

f. Computing regional mean changes

In Section 6, when comparing changes in precipitation variability and means at regional and global scales, we focus on the mean relationships across a region rather than on the relationship of regional means (though we show that results are robust to the metric chosen). We therefore compute the area-weighted geometric average (exponentiated average of the log) of grid-cell-level present-future ratios. This spatial method implicitly weights arid and wet regions equally, since it averages the fractional change of all grid cells regardless of their precipitation amounts. The approach is in line with that of He and Li (2018), but differs from that of Pendergrass et al. (2017), who first average across grid cells and then compute changes in regional mean precipitation. We show in Supplementary Online Materials Section S5 that our conclusions are robust to the method chosen.

4. Results: scale dependence

As discussed previously, in high-resolution future climate simulations with increasing rainfall, the number of dry intervals also robustly increases (Hennessy et al. 1997; Allen and Ingram 2002; Trenberth et al. 2003). An increase in dry intervals necessarily means an amplification of measured

variability over that driven by a simple multiplicative mean change. This constraint is however removed if model output is aggregated beyond the scale of individual events. We would therefore expect that at high resolutions, the relationship between precipitation variability and mean changes would be scale-dependent.

We test the effect of progressive aggregation using high-resolution downscaled WRF-CCSM4 simulations, which allow examining temporal scales from 3-hourly to monthly and spatial scales from 12 km to continental. Figure 1 illustrates the result of aggregation in time for a 108×108 km area in Eastern North America, with distribution changes shown as q-q and quantile ratio plots. In 3-hourly output, distributional changes are complex: precipitation incidences in the upper tail (the strongest rainfall) rise in intensity as Clausius-Clapeyron, while those in the lower tail (the weakest rainfall) actually become less intense, so that the precipitation distribution widens substantially, even when considering only those periods with non-zero precipitation (Figure 1, left column). When precipitation is aggregated over a month, the distributional changes become smaller and simpler, approaching a simple multiplicative shift by the fractional mean change (Figure 1, right column). Behavior is similar even when we consider summer and winter separately (Figures S2-3), or consider only time periods with nonzero precipitation (Figure S4). As expected, this scale dependence can be removed by aggregating in space: in regional precipitation ($\sim 2000 \times 3000$ km), distributional changes are similar at all timescales (Figure S5).

This scale dependence is prevalent in our WRF-CCSM4 simulations. Throughout the simulated domain, changes in precipitation variability substantially exceed those in means at scales that resolve individual precipitation events, but become more similar with aggregation. (Precipitation variability is defined as the standard deviation of the distribution, inclusive of periods with no precipitation.) Figure 2 shows average changes in precipitation means and variability across locations in Eastern North America, at progressively higher levels of aggregation in space and time, from

3-hourly to monthly and 12 to 384 km. (See Figure S6 for maps showing pixel-wise results and Figure S7 for a representation as quantile ratios.) Aggregation over either space or time reduces changes in precipitation variability. This effect is not an artifact of deseasonalizing the timeseries, which affects only values at timescales close to a season (Figure S8, which also shows the similar behavior of the western part of the WRF domain.) It is also not an artifact of the nudging process; in a comparison of similar runs of WRF performed with and without nudging, decreases on aggregation are similar (Figure S9).

The scale-dependence of precipitation variability changes may eventually plateau with sufficient aggregation, as the influence of changes in the organization of individual precipitation events is diminished. Such a plateau is implied by Pendergrass et al. (2017), who found relatively stable behavior in globally averaged precipitation in the CMIP5 multi-model mean, with $\varepsilon_{\sigma} \sim 1.07$ at temporal scales from daily to 3 years. The WRF-CCSM4 simulations shown here cannot be used to find a plateau point, because their short length and limited domain lead to large uncertainties at higher aggregation scales. Instead, we turn to the millennial LongRunMIP runs to evaluate whether the relationship between precipitation variability and mean changes eventually reaches some stable value. We repeat the same analysis for global and Eastern North America precipitation from LongRunMIP models, at timescales of monthly to multi-decadal, and find that the “extra” variability factor ε_{σ} in the multi-model mean is relatively stable, as in Pendergrass et al. (2017). However, individual models may show trends of either sign, due either to differences across models or to uncertainty in individual realizations (Figure S10)

In the remainder of this work, we focus on aggregation scales at which the signature of individual precipitation events is removed. (That is, there are no or very few data without precipitation). We use primarily monthly timescales for both CMIP5 and LongRunMIP, which allows us to directly compare model output from the two archives, though in some cases we compare to results in daily

CMIP5 data. Across the CMIP5 and LongRunMIP models in this analysis, the number of grid-cell-months showing no monthly precipitation is $<0.1\%$ in all but two models. (Exceptions are INM-CM4, which is still $<0.4\%$, and IPSL-CM5A-MR which has 1.8% and 2.1% dry grid-cell-months in control and RCP8.5 CMIP5 simulations.)

5. Results: distributional changes

While recent papers have begun to address distributional changes in precipitation, those studies that have shown an “extra” rise in precipitation variability in future climate conditions have not fully resolved how that change is manifested in precipitation distributions, or how distributional shifts vary across the globe. For example, Pendergrass and Knutti (2018) compared daily precipitation in present-day and future CMIP5 simulations, but did not explicitly model changes in full distributions. The millennial-scale LongRunMIP runs allow evaluating distributional changes with confidence, at least for ~ 1000 km scale regions. Figure 3 compares raw present and future precipitation distributions across the globe in 25 land regions in the CESM model, representative of LongRunMIP (see Figure S11 for ocean regions), and shows also the synthetic distribution corresponding to the simple multiplicative mean shift of Equation 1. The multiplicative mean shift model largely captures distributional changes, though in some cases an extra broadening or even narrowing is clearly evident: wider or narrower true (red) than synthetic (black) distributions. This relatively simple behavior occurs in most LongRunMIP models (Figure S12, see also Section S6 for versions of Figures 3 and S12 for all models). Note that we use annual precipitation here; monthly raw distributions may also be complicated by evolving seasonality; see Figure S13. These effects motivate our decision to deseasonalize precipitation in most analyses.

Figure 3 shows that anomalous changes in precipitation variability clearly differ by region. “Extra broadening” is manifested strongly in locations where future precipitation declines and pre-

precipitation distributions actually narrow: in these conditions ϵ_σ will be > 1 if future distributions narrow *less* than the mean shift would imply. In the CESM land regions of Figure 3, extra broadening is evident in geographically contiguous areas that include a region where future precipitation declines (e.g. W. and Central N. America and Central America, or E., W., and S. Africa). At very high latitudes (Antarctic Land, Arctic Ocean in Figure S11), precipitation consistently rises and extra narrowing ($\epsilon_\sigma < 1$) is more prevalent. Overall, global land shows a 15% increase in mean annual precipitation but a 20% increase in its variability, for an ϵ_σ of 1.05, but ϵ_σ is as high as 1.2 in the four land regions experiencing drying (Central America, Amazonia, South Africa, and the Mediterranean). Ocean regions also show relatively simple distributional changes, but include more regions with extra narrowing, especially in the equatorial Pacific where precipitation means increase strongly but variability does not follow (Figure S7). Overall, the global ocean shows a 10% increase in mean precipitation but almost no net change in variability, for an ϵ_σ of 0.90. The lowest ϵ_σ value, 0.6, occurs in the Equatorial West Pacific, the region with the strongest increase on the Earth. See Tables S1 and S2 for complete information for all regions.

These distributional changes are best highlighted with quantile ratio plots. In a quantile ratio plot, a multiplicative mean shift is manifested as a flat line at $y = \mu_f/\mu_i$, an extra broadening as an upward-sloping line, and an extra narrowing as a downward-sloping one. Figure 4 shows the CESM future precipitation distributions of Figure 3 as quantile ratios relative to the present-day distribution. (See Figure S14 for monthly values, S15 for ocean regions, and Section S6 for other models). For comparison we show also the multiplicative mean shift of Equation 1 (black dot-dashed line) and the synthetic distribution of Equation 2 (turquoise dashed line). The latter transformation modifies the present distribution with a multiplicative and an additive shift based on both the mean change μ_f/μ_i and the extra broadening ϵ_σ , making it necessarily nonlinear and producing a distinctive curved line. Results from an Anderson-Darling test imply that the

future distributional changes in annual precipitation shown here are consistent with this simple two-parameter model, with p-values $> .05$ (global land: 0.27, global ocean: 0.74). For monthly precipitation, evolving seasonality makes distributional changes more complicated and Anderson-Darling p-values are $< .05$. See Tables S1 and S2 for all values and regions. The relatively simple distributional transformations suggest that changes in aggregated precipitation are governed by fundamental principles, at least in models.

6. Results: variability changes at grid-cell level

To better understand the geographic diversity of changes in precipitation, we consider changes at the grid-cell scale. As seen in Section 4, aggregation to the typical model spatial resolution order of ~ 100 km is sufficient to remove the signature of individual precipitation events in monthly and possibly even daily precipitation. (Deseasonalizing removes any effect of seasonal changes.) Because the analysis of Section 5 suggests that distributional changes are relatively simple, we simplify analysis by considering only a single metric of variability, the standard deviation. Comparing changes in standard deviation to those in means then allows us to understand the factors governing the extra broadening ϵ_{σ} .

Models robustly show highly correlated precipitation mean and variability changes with distinct spatial patterns. Figure 5a shows representative LongRunMIP and CMIP5 models; see Figure S16 for all models. The geographic pattern of precipitation increases in the tropics and high-latitudes and declines in the subtropics has been well known for decades (Hennessy et al. 1997; Räisänen 2002; Allen and Ingram 2002), and the similarity between mean and variability changes has also been widely acknowledged (Rind et al. 1988; Groisman et al. 1999). We use the LongRunMIP archive to quantify these relationships with high confidence even at interannual timescales. In the shorter CMIP5 model runs, changes even in sub-annual precipitation variability are not significant

over much of the Earth, and evaluating interannual changes is problematic: compare rows in Figure 5a, which uses 500 year segments in LongRunMIP runs, vs. 30 years in CMIP5 (see Figure S16 for all models). Stippling marks grid cells with non-significant changes, calculated as described in Section 3e.

In all models, precipitation changes in individual locations can be very large, rising or falling by a factor of 2 or more, and changes in variability largely follow those in means (Figure 5b, which shows both LongRunMIP and CMIP5 models and both sub-annual and interannual variability; see Figure S17 for remaining models.) The global average changes in mean and variability in each model are small (black dots in Figure 5b), as they average over both wetting and drying locations. We also show in Figure 5b fits of the relationship between changes in precipitation means and variability across locations in each model, assuming a linear dependence:

$$\log\left(\frac{\sigma_f}{\sigma_i}\right) = \alpha + \beta \cdot \log\left(\frac{\mu_f}{\mu_i}\right) \quad (3)$$

Like our two-parameter model for distributional shifts, Equation 3 contains an additive and a multiplicative component. The predicted local extra broadening $\hat{\epsilon}_\sigma$ is a function of the mean change if $\beta \neq 1$:

$$\log \hat{\epsilon}_\sigma = \alpha + (\beta - 1) \cdot \log\left(\frac{\mu_f}{\mu_i}\right) \quad (4)$$

The global mean $\frac{1}{\sqrt{2}} \overline{\log \epsilon_\sigma}$ is the orthogonal distance from this 1:1 line to the black dots marking global mean changes.

Several features in Figure 5b are universal or near-universal across models and frequencies. In all models, precipitation variability changes are highly correlated with those in means. Nearly all models also show a non-zero intercept α of the fit to Equation 3, i.e. a slight increase in future pre-

cipitation variability even where mean changes are negligible. This condition follows when global $\bar{\epsilon}_\sigma > 1$. (Similar results were found by Pendergrass et al. (2017).) In nearly all cases, this extra variability component lessens with increasing precipitation mean change, i.e. the slope $\beta < 1$. Figure 6 shows slopes, correlation coefficients, and ϵ_σ for all 12 CMIP5 and 6 LongRunMIP models, and Table S3 provides all values. Results are robust across models in both CMIP5 and LongRunMIP archives. The most appropriate comparison is for subannual variability, since CMIP5 models have large fit uncertainty for interannual variability. (They also show larger slopes and lower correlations.) For subannual variability, the average $\bar{\epsilon}_\sigma$ is 1.05 for both LongRunMIP and CMIP5 models, with a total range 0.94–1.12 and only two models below 1 (CCSM3 and MIROC-ESM). The average slope β is 0.79 and 0.91 for LongRunMIP and CMIP5 models, respectively, with only a single CMIP5 model showing $\beta > 1$ (BCC-CSM 1.1). For comparison of a single model in both archives, see Figure S18. Results are also robust across individual seasons (Figure S19) and whether daily or monthly precipitation is used (Figure S20). The combination of a positive offset in global average variability ($\bar{\epsilon}_\sigma > 1$) with a negative dependence on precipitation changes ($\beta < 1$) means that changes to precipitation distributions vary regionally. Precipitation distributions tend to narrow less than expected in drying regions, broaden slightly where mean changes are zero, and broaden less than expected where precipitation increases strongly. To highlight these results, we show in Figure 7 model mean and variability changes for different regions (global, subtropics, and high latitudes), along with the fitted across-pixel relationships. As discussed above, globally averaged changes involve a slight extra broadening $\bar{\epsilon}_\sigma$ in all but two models (Figure 7 top, mean across models 1.05). The subtropics (20–35°), which typically dry, involve still larger $\bar{\epsilon}_\sigma$ (bottom left, mean across models 1.12). The high latitudes (55–90°), which universally experience large precipitation increases, show $\bar{\epsilon}_\sigma < 1$ (bottom right, mean 0.96). This framework clarifies previous findings that high latitude regions generally do not show extra broadening of precipitation distri-

butions (Hennessy et al. 1997; Pendergrass et al. 2017; O’Gorman and Schneider 2009; Groisman et al. 1999).

The global negative dependence of extra broadening on precipitation changes does not always apply within individual regions. While the mean global slope β across all models in Figure 7 is 0.87 (standard deviation 0.10), regional slopes in the subtropics and high latitudes are close to unity: 1.02 ($\sigma = 0.18$) and 0.95 ($\sigma = 0.17$), respectively. Results for the subtropics are consistent with those of He and Li (2018), who find in climatological descending regions a slope of 0.99 across all pixels in 30 CMIP5 models, with a positive intercept. The global dependence on precipitation change is evidently driven primarily by behavior in the midlatitudes (slope 0.77) and to some extent the tropics (0.90). The same regional pattern holds when either CMIP5 or LongRunMIP models are considered separately.

These results expand on the findings of Pendergrass et al. (2017), and when averaged globally are consistent with that work. Our global mean $\bar{\epsilon}_\sigma$ of 1.05 for subannual variability across CMIP5 models is similar to the ~ 1.06 inferred in Pendergrass et al. (2017) with slightly different choices in analysis. We use monthly precipitation over the entire Earth and compute the mean of fractional precipitation changes; Pendergrass et al. (2017) use daily precipitation for global land only at frequencies from 1 day to 3 years, and compute the fractional change in mean precipitation. Results are insensitive to these choices: daily and monthly precipitation values are nearly identical, as shown in Figures 7 and S20, and choice of averaging method or restriction to land only (Figures S21–S23) also have only small effects.

Note that global values may be only minimally relevant to local impacts of future precipitation changes. Global values average over areas of both wetting and drying and are therefore small relative to changes manifested at individual locations. Globally, mean precipitation changes are 1.4–5.6%/K, but local precipitation changes can be much larger: the 0.05-0.95 inter-quartile range

exceeds 25%/K for most models, and 44%/K for MPI-ESM-LR. In a global or even large-scale regional analysis, aggregated precipitation behavior will be dominated by extra broadening effects: in Equation 3, the intercept α is large relative to the mean change term $\beta \cdot \log(\mu_f/\mu_i)$. Locally, however, estimated changes in precipitation variability will typically be dominated by the mean change term.

Similarity of variability changes across timescales.

The millennial-scale LongRunMIP data also allow us to examine whether and how changes in precipitation variability differ across timescales. The above analysis of changes in variability and means suggests little frequency dependence (slopes for subannual and inter-annual variability are similar in Figure 6 for LongRunMIP models, which can better resolve interannual precipitation patterns). To more carefully examine the question of scale-dependence, we now directly compare subannual and interannual variability changes for the 6 LongRunMIP models (Figure 8).

Outside the tropics, changes in precipitation variability appear nearly independent of the timescale of variability. Variability changes across frequencies are highly correlated and nearly identical: correlation coefficients and slopes are close to 1, closer than equivalent values obtained when comparing changes in variability and means. That is, changes in interannual and subannual precipitation variability are more similar to each other than they are to mean changes.

Within the tropics, interannual variability changes are lower than subannual changes in all models other than MPI-ESM-12. While the geographic patterns of the relationship are complex, producing scatter in the relationship (mean correlation coefficient 0.66), the frequency distinction is strongest in the tropical Pacific. Across non-MPI models, tropical Pacific mean precipitation increases by an average of 18%, subannual variability by 21%, and interannual variability only by 17%. The effect is likely related to a dampened ENSO: Callahan et al. (2019) find that future ENSO amplitude declines in all LongRunMIP models other than those in the MPI family.

7. Conclusions

The systematic multi-scale analysis of precipitation variability changes presented here harmonizes and expands on prior studies performed at more restricted temporal and spatial scales. The use of millennial-scale LongRunMIP simulations allows explicitly modeling distributional changes in regional precipitation, which is problematic with noisier output from shorter simulations, and evaluation of changes on timescales as long as multi-decadal. Primary results fall into four categories: scale dependence in high-resolution model output, modeling of distributional changes, regional dependence of distributional changes, and frequency independence. Results are remarkably consistent across models, suggesting that they are governed by fundamental physical principles.

Scale-dependence. Physical constraints on the hydrological cycle lead to the well-known amount/intensity discrepancy in future precipitation changes ($\sim 7\%/K$ rise in intensity but only $\sim 2\%/K$ rise in total amount). The discrepancy results in longer dry spells between precipitation incidences, and means that precipitation variability changes should be larger than mean changes if individual precipitation events are resolved. We show in dynamically downscaled WRF-CCSM simulations that this event-scale excess variability is indeed present and that it reduces with either spatial or temporal aggregation beyond event scale. That is, at high resolution, precipitation variability changes are scale-dependent in their relationship to changes in the mean. The effects of changes in the organization of individual events are effectively removed at monthly, ~ 200 km aggregation and likely also at the daily, ~ 100 km scale typical of GCM output.

Modeling distributional changes. Once aggregated well beyond event scale, we find that precipitation distributions are well-described by a two-parameter model combining a multiplicative shift by the mean change and a small “extra” variability parameter ε_{σ} . As in prior studies, we find that

in the global average, this “extra” variability change is slightly above 1, meaning that precipitation variability increases on average slightly more than the increase in mean precipitation. For most locations, however, precipitation variability changes are dominated by the mean change term.

Regional dependence. A similar 2-parameter model can be used to fit the relationship of variability changes across space. In nearly all models the slope of this relationship, describing the strength of the multiplicative shift, is slightly below 1, and the additive term is above 1. That is, the extra variability ε_{σ} is largest in regions that become drier. As a result, precipitation distributions narrow less than expected from the mean change in drying regions, broaden slightly more than expected where mean changes are zero, and broaden less than expected where precipitation increases strongly.

Frequency independence. Millennial-scale simulations allow us to show that outside the tropics, changes in model precipitation variability are nearly identical on timescales from monthly to multi-decadal. We see no evidence for an additional amplification of low-frequency variability. In the tropical Pacific, increases in interannual precipitation variability are generally lower than those in sub-annual variability and likely reflect a dampened ENSO.

The combined results above show the power of studies that span multiple scales, and suggest avenues for future work. First, in this work we have removed the seasonal cycle to focus on non-seasonal precipitation variability, but this analysis framework can also be applied to investigate shifts in seasonality itself. Second, while many studies on future precipitation variability focus on wet extremes (the upper tail of precipitation distributions) in regions becoming wetter, results here imply that the lower tail of regions becoming drier should also raise concerns. Societal impacts may be significant if the driest periods sampled become drier even than implied by the mean shift. The simulations of drying regions shown in this work do show this behavior, but more systematic assessment is needed. In general, millennial-scale climate simulations now allow detailed

analysis of distributional changes in model precipitation that would imply detrimental societal consequences. Several other areas are also obvious needs. The analysis here is primarily descriptive, characterizing changes in model simulations of future precipitation. Because the changes identified are highly robust across models, it should be possible to explain them as outcomes of an underlying physical mechanism. Finally, it is important to understand how representative these model changes are of the real world. Interest is growing in evaluating distributional changes in observed precipitation. The increasing availability of both high-resolution simulations and well-sampled coarser ones (as millennial-scale runs or ensembles) can support cross-scale studies to assess projections of precipitation changes.

Acknowledgments. The authors thank Michael Stein, Won Chang, Jessica Kunke, and Victor Zhorin for helpful comments and suggestions. This work was conducted as part of the Center for Robust Decision-making on Climate and Energy Policy (RDCEP) at the University of Chicago, supported by the NSF Decision Making Under Uncertainty program, NSF grant #SES-1463644. This work was completed in part with resources provided by the University of Chicago Research Computing Center.

References

- Abghari, H., H. Tabari, and P. Hosseinzadeh Talaei, 2013: River flow trends in the west of Iran during the past 40years: Impact of precipitation variability. *Global and Planetary Change*, **101**, 52–60, doi:10.1016/j.gloplacha.2012.12.003, URL <http://www.sciencedirect.com/science/article/pii/S0921818112002317>.
- Allen, M. R., and W. J. Ingram, 2002: Constraints on future changes in climate and the hydrologic cycle. *Nature*, **419** (6903), 224–232, doi:10.1038/nature01092, URL <http://www.nature.com/>

nature/journal/v419/n6903/abs/nature01092.html.

Ault, T. R., J. E. Cole, and S. S. George, 2012: The amplitude of decadal to multidecadal variability in precipitation simulated by state-of-the-art climate models. *Geophysical Research Letters*, **39** (21), doi:10.1029/2012GL053424, URL <https://agupubs.onlinelibrary.wiley.com/doi/abs/10.1029/2012GL053424>, eprint: <https://agupubs.onlinelibrary.wiley.com/doi/pdf/10.1029/2012GL053424>.

Barlow, M., S. Nigam, and E. H. Berbery, 2001: ENSO, Pacific Decadal Variability, and U.S. Summertime Precipitation, Drought, and Stream Flow. *Journal of Climate*, **14** (9), 2105–2128, doi:10.1175/1520-0442(2001)014<2105:EPDVAU>2.0.CO;2, URL <https://journals-ametsoc-org.proxy.uchicago.edu/doi/abs/10.1175/1520-0442%282001%29014%3C2105%3AEPDVAU%3E2.0.CO%3B2>.

Bellenger, H., E. Guilyardi, J. Leloup, M. Lengaigne, and J. Vialard, 2014: ENSO representation in climate models: from CMIP3 to CMIP5. *Climate Dynamics*, **42** (7), 1999–2018, doi:10.1007/s00382-013-1783-z, URL <https://link.springer.com/article/10.1007/s00382-013-1783-z>, company: Springer Distributor: Springer Institution: Springer Label: Springer Number: 7 Publisher: Springer Berlin Heidelberg.

Biasutti, M., 2013: Forced Sahel rainfall trends in the CMIP5 archive. *Journal of Geophysical Research: Atmospheres*, **118** (4), 1613–1623, doi:10.1002/jgrd.50206, URL <https://agupubs.onlinelibrary.wiley.com/doi/abs/10.1002/jgrd.50206>, eprint: <https://agupubs.onlinelibrary.wiley.com/doi/pdf/10.1002/jgrd.50206>.

Brown, J. R., A. F. Moise, and R. A. Colman, 2017: Projected increases in daily to decadal variability of Asian-Australian monsoon rainfall. *Geophysical Research Letters*, **44** (11), 5683–5690, doi:10.1002/2017GL073217, URL

<https://agupubs.onlinelibrary.wiley.com/doi/abs/10.1002/2017GL073217>, _eprint:
<https://agupubs.onlinelibrary.wiley.com/doi/pdf/10.1002/2017GL073217>.

Callahan, C. W., C. Chen, M. Rugenstein, J. Bloch-Johnson, S. Yang, and E. J. Moyer, 2019: Robust decrease in ENSO amplitude under long-term warming. *Nature Climate Change*, (**submitted**).

Castruccio, S., D. J. McInerney, M. L. Stein, F. L. Crouch, R. L. Jacob, and E. J. Moyer, 2013: Statistical Emulation of Climate Model Projections Based on Precomputed GCM Runs. *Journal of Climate*, **27** (5), 1829–1844, doi:10.1175/JCLI-D-13-00099.1, URL <http://journals.ametsoc.org/doi/abs/10.1175/JCLI-D-13-00099.1>.

Chang, W., M. L. Stein, J. Wang, V. R. Kotamarthi, and E. J. Moyer, 2016: Changes in Spatiotemporal Precipitation Patterns in Changing Climate Conditions. *Journal of Climate*, **29** (23), 8355–8376, doi:10.1175/JCLI-D-15-0844.1, URL <http://journals.ametsoc.org/doi/abs/10.1175/JCLI-D-15-0844.1>.

Chang, W., J. Wang, J. Marohnic, V. R. Kotamarthi, and E. J. Moyer, 2018: Diagnosing added value of convection-permitting regional models using precipitation event identification and tracking. *Climate Dynamics*, doi:10.1007/s00382-018-4294-0, URL <https://doi.org/10.1007/s00382-018-4294-0>.

Chen, C., W. Chang, J. Wang, V. R. Kotamarthi, W. Kong, M. L. Stein, and E. J. Moyer, 2020: Convective precipitation events intensify but contract under global warming. *Nature Climate Change*, (**submitted**).

Cheung, A. H., M. E. Mann, B. A. Steinman, L. M. Frankcombe, M. H. England, and S. K. Miller, 2017: Comparison of Low-Frequency Internal Climate Variability

in CMIP5 Models and Observations. *Journal of Climate*, **30** (12), 4763–4776, doi: 10.1175/JCLI-D-16-0712.1, URL <https://journals.ametsoc.org/jcli/article/30/12/4763/98057/Comparison-of-Low-Frequency-Internal-Climate>, publisher: American Meteorological Society.

Covey, C., P. J. Gleckler, C. Doutriaux, D. N. Williams, A. Dai, J. Fasullo, K. Trenberth, and A. Berg, 2016: Metrics for the Diurnal Cycle of Precipitation: Toward Routine Benchmarks for Climate Models. *Journal of Climate*, **29** (12), 4461–4471, doi:10.1175/JCLI-D-15-0664.1, URL <https://journals.ametsoc.org/doi/full/10.1175/JCLI-D-15-0664.1>, publisher: American Meteorological Society.

Dai, A., 2006: Precipitation Characteristics in Eighteen Coupled Climate Models. *Journal of Climate*, **19** (18), 4605–4630, doi:10.1175/JCLI3884.1, URL <https://journals.ametsoc.org/doi/full/10.1175/JCLI3884.1>, publisher: American Meteorological Society.

Dai, A., R. M. Rasmussen, C. Liu, K. Ikeda, and A. F. Prein, 2017: A new mechanism for warm-season precipitation response to global warming based on convection-permitting simulations. *Climate Dynamics*, doi:10.1007/s00382-017-3787-6, URL <https://doi.org/10.1007/s00382-017-3787-6>.

Davini, P., and C. Cagnazzo, 2014: On the misinterpretation of the North Atlantic Oscillation in CMIP5 models. *Climate Dynamics*, **43** (5), 1497–1511, doi:10.1007/s00382-013-1970-y, URL <https://doi.org/10.1007/s00382-013-1970-y>.

Emanuel, K. A., 2013: Downscaling CMIP5 climate models shows increased tropical cyclone activity over the 21st century. *Proceedings of the National Academy of Sciences*, **110** (30), 12 219–12 224, doi:10.1073/pnas.1301293110, URL <https://www.pnas.org/content/110/30/12219>, publisher: National Academy of Sciences Section: Physical Sciences.

- Eyring, V., and Coauthors, 2019: Taking climate model evaluation to the next level. *Nature Climate Change*, **9** (2), 102–110, doi:10.1038/s41558-018-0355-y, URL <https://www.nature.com/articles/s41558-018-0355-y>, number: 2 Publisher: Nature Publishing Group.
- Frost, C., and S. G. Thompson, 2000: Correcting for Regression Dilution Bias: Comparison of Methods for a Single Predictor Variable. *Journal of the Royal Statistical Society. Series A (Statistics in Society)*, **163** (2), 173–189, URL www.jstor.org/stable/2680496.
- Fuentes-Franco, R., F. Giorgi, E. Coppola, and F. Kucharski, 2016: The role of ENSO and PDO in variability of winter precipitation over North America from twenty first century CMIP5 projections. *Climate Dynamics*, **46** (9), 3259–3277, doi:10.1007/s00382-015-2767-y, URL <https://doi.org/10.1007/s00382-015-2767-y>.
- Gornall, J., R. Betts, E. Burke, R. Clark, J. Camp, K. Willett, and A. Wiltshire, 2010: Implications of climate change for agricultural productivity in the early twenty-first century. *Philosophical Transactions of the Royal Society of London B: Biological Sciences*, **365** (1554), 2973–2989, doi:10.1098/rstb.2010.0158, URL <http://rstb.royalsocietypublishing.org/content/365/1554/2973>.
- Goyal, M. K., C. S. P. Ojha, and D. H. Burn, 2012: Nonparametric Statistical Downscaling of Temperature, Precipitation, and Evaporation in a Semiarid Region in India. *Journal of Hydrologic Engineering*, **17** (5), 615–627, doi:10.1061/(ASCE)HE.1943-5584.0000479, URL <https://ascelibrary.org/doi/full/10.1061/%28ASCE%29HE.1943-5584.0000479>, publisher: American Society of Civil Engineers.
- Groisman, P. Y., and Coauthors, 1999: Changes in the Probability of Heavy Precipitation: Important Indicators of Climatic Change. *Climatic Change*, **42** (1), 243–283, doi:10.1023/A:1005432803188, URL <https://link.springer.com/article/10.1023/A:1005432803188>.

- Hamlet, A. F., P. W. Mote, M. P. Clark, and D. P. Lettenmaier, 2005: Effects of Temperature and Precipitation Variability on Snowpack Trends in the Western United States. *Journal of Climate*, **18** (21), 4545–4561, doi:10.1175/JCLI3538.1, URL <http://journals.ametsoc.org/doi/abs/10.1175/JCLI3538.1>.
- He, C., and T. Li, 2018: Does global warming amplify interannual climate variability? *Climate Dynamics*, 1–18, doi:10.1007/s00382-018-4286-0, URL <https://link.springer.com/article/10.1007/s00382-018-4286-0>.
- Hennessy, K. J., J. M. Gregory, and J. F. B. Mitchell, 1997: Changes in daily precipitation under enhanced greenhouse conditions. *Climate Dynamics*, **13** (9), 667–680, doi:10.1007/s003820050189, URL <https://link.springer.com/article/10.1007/s003820050189>.
- Hunt, B. G., and T. I. Elliott, 2004: Interaction of climatic variability with climatic change. *Atmosphere-Ocean*, **42** (3), 145–172, doi:10.3137/ao.420301, URL <https://doi.org/10.3137/ao.420301>.
- Ines, A. V. M., and J. W. Hansen, 2006: Bias correction of daily GCM rainfall for crop simulation studies. *Agricultural and Forest Meteorology*, **138** (1), 44–53, doi:10.1016/j.agrformet.2006.03.009, URL <http://www.sciencedirect.com/science/article/pii/S0168192306000979>.
- Katz, R. W., and B. G. Brown, 1992: Extreme events in a changing climate: Variability is more important than averages. *Climatic Change*, **21** (3), 289–302, doi:10.1007/BF00139728, URL <https://link.springer.com/article/10.1007/BF00139728>.
- Klavans, J. M., A. Poppick, S. Sun, and E. J. Moyer, 2016: The influence of model resolution on temperature variability. *Climate Dynamics*, 1–11, doi:10.1007/s00382-016-3249-6, URL <https://link.springer.com/article/10.1007/s00382-016-3249-6>.

- Knutti, R., D. Masson, and A. Gettelman, 2013: Climate model genealogy: Generation CMIP5 and how we got there. *Geophysical Research Letters*, **40** (6), 1194–1199, doi:10.1002/grl.50256, URL <http://onlinelibrary.wiley.com/doi/10.1002/grl.50256/abstract>.
- Kripalani, R. H., J. H. Oh, A. Kulkarni, S. S. Sabade, and H. S. Chaudhari, 2007: South Asian summer monsoon precipitation variability: Coupled climate model simulations and projections under IPCC AR4. *Theoretical and Applied Climatology*, **90** (3-4), 133–159, doi:10.1007/s00704-006-0282-0, URL <http://link.springer.com/article/10.1007/s00704-006-0282-0>.
- Liang, X.-Z., W.-C. Wang, and M. P. Dudek, 1995: Interannual variability of regional climate and its change due to the greenhouse effect. *Global and Planetary Change*, **10** (1), 217–238, doi:10.1016/0921-8181(94)00027-B, URL <http://www.sciencedirect.com/science/article/pii/092181819400027B>.
- Lu, R., and Y. Fu, 2010: Intensification of East Asian Summer Rainfall Interannual Variability in the Twenty-First Century Simulated by 12 CMIP3 Coupled Models. *Journal of Climate*, doi:<http://dx.doi.org/10.1175/2009JCLI3130.1>, URL <https://journals.ametsoc.org/doi/10.1175/2009JCLI3130.1>.
- Maher, N., D. Matei, S. Milinski, and J. Marotzke, 2018: ENSO Change in Climate Projections: Forced Response or Internal Variability? *Geophysical Research Letters*, **45** (20), 11,390–11,398, doi:10.1029/2018GL079764, URL <https://agupubs.onlinelibrary.wiley.com/doi/abs/10.1029/2018GL079764>, eprint: <https://agupubs.onlinelibrary.wiley.com/doi/pdf/10.1029/2018GL079764>.
- Mearns, L. O., F. Giorgi, L. McDaniel, and C. Shields, 1995: Analysis of daily variability of precipitation in a nested regional climate model: comparison with observations and doubled CO₂

results. *Global and Planetary Change*, **10** (1), 55–78, doi:10.1016/0921-8181(94)00020-E, URL <http://www.sciencedirect.com/science/article/pii/092181819400020E>.

Meehl, G. A., M. Wheeler, and W. M. Washington, 1994: Low-frequency variability and CO₂ transient climate change. Part 3. Intermonthly and interannual variability. *Climate Dynamics*, **10** (6), 277–303, doi:10.1007/BF00228028, URL <https://doi.org/10.1007/BF00228028>.

O’Gorman, P. A., and T. Schneider, 2009: The physical basis for increases in precipitation extremes in simulations of 21st-century climate change. *Proceedings of the National Academy of Sciences*, **106** (35), 14 773–14 777, doi:10.1073/pnas.0907610106, URL <http://www.pnas.org/content/106/35/14773>.

Pendergrass, A. G., and D. L. Hartmann, 2014: Two Modes of Change of the Distribution of Rain. *Journal of Climate*, **27** (22), 8357–8371, doi:10.1175/JCLI-D-14-00182.1, URL <http://journals.ametsoc.org/doi/abs/10.1175/JCLI-D-14-00182.1>.

Pendergrass, A. G., and R. Knutti, 2018: The Uneven Nature of Daily Precipitation and Its Change. *Geophysical Research Letters*, **45** (21), 11,980–11,988, doi:10.1029/2018GL080298, URL <https://agupubs-onlinelibrary-wiley-com.ezproxy.cul.columbia.edu/doi/10.1029/2018GL080298>.

Pendergrass, A. G., R. Knutti, F. Lehner, C. Deser, and B. M. Sanderson, 2017: Precipitation variability increases in a warmer climate. *Scientific Reports*, **7** (1), 17 966, doi:10.1038/s41598-017-17966-y, URL <https://www.nature.com/articles/s41598-017-17966-y>.

Polade, S. D., A. Gershunov, D. R. Cayan, M. D. Dettinger, and D. W. Pierce, 2013: Natural climate variability and teleconnections to precipitation over the Pacific-North American region in CMIP3 and CMIP5 models. *Geophysical Research Letters*, **40** (10), 2296–

2301, doi:10.1002/grl.50491, URL <https://agupubs.onlinelibrary.wiley.com/doi/abs/10.1002/grl.50491>, eprint: <https://agupubs.onlinelibrary.wiley.com/doi/pdf/10.1002/grl.50491>.

Räisänen, J., 2002: CO₂-Induced Changes in Interannual Temperature and Precipitation Variability in 19 CMIP2 Experiments. *Journal of Climate*, **15** (17), 2395–2411, doi:10.1175/1520-0442(2002)015<2395:CICIIT>2.0.CO;2.

Riha, S. J., D. S. Wilks, and P. Simoens, 1996: Impact of temperature and precipitation variability on crop model predictions. *Climatic Change*, **32** (3), 293–311, doi:10.1007/BF00142466, URL <https://link.springer.com/article/10.1007/BF00142466>.

Rind, D., R. Goldberg, and R. Ruedy, 1988: Change in climate variability in the 21st century. *Climatic Change*, **14** (1), 5–37, URL <https://link-springer-com.proxy.uchicago.edu/article/10.1007/BF00140173>.

Rugenstein, M., and Coauthors, 2019: LongRunMIP – motivation and design for a large collection of millennial-length AO-GCM simulations. *Bulletin of the American Meteorological Society*, doi:10.1175/BAMS-D-19-0068.1, URL <https://journals.ametsoc.org/doi/abs/10.1175/BAMS-D-19-0068.1>.

Rupp, D. E., J. T. Abatzoglou, K. C. Hegewisch, and P. W. Mote, 2013: Evaluation of CMIP5 20th century climate simulations for the Pacific Northwest USA. *Journal of Geophysical Research: Atmospheres*, **118** (19), 10,884–10,906, doi:10.1002/jgrd.50843, URL <https://agupubs.onlinelibrary.wiley.com/doi/abs/10.1002/jgrd.50843>, eprint: <https://agupubs.onlinelibrary.wiley.com/doi/pdf/10.1002/jgrd.50843>.

Semenov, V., and L. Bengtsson, 2002: Secular trends in daily precipitation characteristics: greenhouse gas simulation with a coupled AOGCM. *Climate Dynamics*, **19** (2), 123–140, doi:10.

1007/s00382-001-0218-4, URL <https://link.springer.com/article/10.1007/s00382-001-0218-4>.

Skamarock, W. C., and Coauthors, 2008: A Description of the Advanced Research WRF Version 3. *NCAR Tech*, (Note NCAR/TN-47STR), 113, URL http://www2.mmm.ucar.edu/wrf/users/citing_wrf.html.

Sun, F., M. L. Roderick, and G. D. Farquhar, 2012: Changes in the variability of global land precipitation. *Geophysical Research Letters*, **39** (19), doi:10.1029/2012GL053369, URL <https://agupubs.onlinelibrary.wiley.com/doi/abs/10.1029/2012GL053369>.

Sun, Y., S. Solomon, A. Dai, and R. W. Portmann, 2006: How Often Does It Rain? *Journal of Climate*, **19** (6), 916–934, doi:10.1175/JCLI3672.1, URL <https://journals.ametsoc.org/doi/full/10.1175/JCLI3672.1>, publisher: American Meteorological Society.

Sun, Y., S. Solomon, A. Dai, and R. W. Portmann, 2007: How Often Will It Rain? *Journal of Climate*, **20** (19), 4801–4818, doi:10.1175/JCLI4263.1, URL <http://journals.ametsoc.org/doi/abs/10.1175/JCLI4263.1>.

Taylor, K. E., R. J. Stouffer, and G. A. Meehl, 2011: An Overview of CMIP5 and the Experiment Design. *Bulletin of the American Meteorological Society*, **93** (4), 485–498, doi:10.1175/BAMS-D-11-00094.1, URL <http://journals.ametsoc.org/doi/abs/10.1175/BAMS-D-11-00094.1>.

Trenberth, K. E., A. Dai, R. M. Rasmussen, and D. B. Parsons, 2003: The Changing Character of Precipitation. *Bulletin of the American Meteorological Society*, **84** (9), 1205–1217, doi:10.1175/BAMS-84-9-1205, URL <http://journals.ametsoc.org/doi/abs/10.1175/BAMS-84-9-1205>.

Trenberth, K. E., Y. Zhang, and M. Gehne, 2017: Intermittency in Precipitation: Duration, Frequency, Intensity, and Amounts Using Hourly Data. *Journal of Hydrometeorology*,

18 (5), 1393–1412, doi:10.1175/JHM-D-16-0263.1, URL <https://journals.ametsoc.org/doi/full/10.1175/JHM-D-16-0263.1>, publisher: American Meteorological Society.

van Vuuren, D. P., and Coauthors, 2011: The representative concentration pathways: an overview. *Climatic Change*, **109 (1-2)**, 5, doi:10.1007/s10584-011-0148-z, URL <https://link.springer.com/article/10.1007/s10584-011-0148-z>.

Vitart, F., A. W. Robertson, and D. L. T. Anderson, 2012: Subseasonal to Seasonal Prediction Project: bridging the gap between weather and climate. *WMO Bulletin*, **61 (2)**, URL https://www.researchgate.net/profile/Frederic_Vitart/publication/233867073_Subseasonal_to_Seasonal_Prediction_Project_Bridging_the_gap_between_weather_and_climate/links/0c960518b9e4c0acc4000000/Subseasonal-to-Seasonal-Prediction-Project-Bridging-the-gap-between-weather-and-climate.pdf.

Wang, J., and V. R. Kotamarthi, 2015: High-resolution dynamically downscaled projections of precipitation in the mid and late 21st century over North America. *Earth's Future*, **3 (7)**, 2015EF000 304, doi:10.1002/2015EF000304, URL <http://onlinelibrary.wiley.com/doi/10.1002/2015EF000304/abstract>.

Wasko, C., A. Sharma, and S. Westra, 2016: Reduced spatial extent of extreme storms at higher temperatures. *Geophysical Research Letters*, **43 (8)**, 4026–4032, doi:10.1002/2016GL068509, URL <https://agupubs.onlinelibrary.wiley.com/doi/abs/10.1002/2016GL068509>.

Wetherald, R. T., 2010: Changes of time mean state and variability of hydrology in response to a doubling and quadrupling of CO₂. *Climatic Change*, **102 (3)**, 651–670, doi:10.1007/s10584-009-9701-4, URL <https://doi.org/10.1007/s10584-009-9701-4>.

Yokoyama, C., and Y. N. Takayabu, 2008: A Statistical Study on Rain Characteristics of Tropical Cyclones Using TRMM Satellite Data. *Monthly Weather Review*, **136** (10), 3848–3862, doi:10.1175/2008MWR2408.1, URL <https://journals.ametsoc.org/mwr/article/136/10/3848/103781/A-Statistical-Study-on-Rain-Characteristics-of>, publisher: American Meteorological Society.

Zwiers, F. W., and V. V. Kharin, 1998: Changes in the Extremes of the Climate Simulated by CCC GCM2 under CO2 Doubling. *Journal of Climate*, **11** (9), 2200–2222, doi:10.1175/1520-0442(1998)011<2200:CITEOT>2.0.CO;2, URL <https://journals.ametsoc.org/doi/10.1175/1520-0442%281998%29011%3C2200%3ACITEOT%3E2.0.CO%3B2>.

APPENDIX

LIST OF TABLES

Table 1. Ensemble of models used for this study	41
Table A1. Description of region codes used in Figures 3, 4, S5-S15, and Section S6	42

TABLE 1. Ensemble of models used for this study

Model Name	Institution	Resolution	Years
<i>Dynamically-downscaled high-resolution model (historical climate, RCP8.5 runs)</i>			
WRF-ARW	National Center for Atmospheric Research, U.S. (NCAR)	12 km × 12 km	10
<i>CMIP5 models (pre-industrial control, RCP8.5 runs)</i>			
ACCESS1-3	Commonwealth Scientific and Industrial Research Organisation, Australia (CSIRO) and Bureau of Meteorology, Australia	1.25° × 1.875°	30
BCC-CSM1.1	Beijing Climate Center, China Meteorological Administration	2.79° × 2.81°	30
CanESM2	Canadian Centre for Climate Modelling and Analysis	2.79° × 2.81°	30
CCSM4	National Center for Atmospheric Research, U.S. (NCAR)	0.94° × 1.25°	30
CSIRO-Mk3-6-0	CSIRO in collaboration with the Queensland Climate Change Centre of Excellence, Australia	1.87° × 1.88°	30
GFDL-CM3	Geophysical Fluid Dynamics Laboratory, U.S. (GFDL)	2° × 2.5°	30
INM-CM4	Institute for Numerical Mathematics, Russia	1.5° × 2°	30
IPSL-CM5A-MR	Institut Pierre-Simon Laplace, France (IPSL)	1.27° × 2.5°	30
MIROC-ESM	Japan Agency for Marine-Earth Science and Technology, Atmosphere and Ocean Research Institute (The University of Tokyo) and National Institute for Environmental Studies	2.79° × 2.81°	30
MPI-ESM-LR	Max Planck Institute for Meteorology, Germany (MPI-M)	1.87° × 1.88°	30
MRI-CGCM3	Meteorological Research Institute, Japan	1.12° × 1.13°	30
NorESM1-M	Norwegian Climate Centre	1.89° × 2.5°	30
<i>LongRunMIP models (pre-industrial control, abrupt 4 × CO₂ runs unless otherwise specified)</i>			
CCSM3 I	NCAR	3.75° × 3.75°	1000
CCSM3 II	NCAR (<i>alt. scenario: abrupt jump from 289–1400 ppm CO₂</i>)	3.75° × 3.75°	2120
CESM 1.0.4	NCAR	1.89° × 2.5°	3765
GISS-E2-R	Goddard Institute for Space Sciences, U.S.	2° × 2.5°	5001
HadCM3L	Hadley Centre for Climate Prediction and Research, U.K.	2.5° × 3.75°	1000
IPSL-CM5A	IPSL	1.89° × 3.75°	1000
MPI-ESM 1.2	MPI-M	1.87° × 1.88°	1000

Table A1. Description of region codes used in Figures 3, 4, S5-S15, and Section S6

Land		Ocean	
ID	Description	ID	Description
ALA	Alaska and Western Canada	AOI	Southern Ocean - Indian/Atlantic
AMZ	Amazonia	AOP	Southern Ocean - Pacific
ANL	Antarctic Land	ARO	Arctic Ocean
ARL	Arctic Land	CAR	Caribbean
CAM	Central America	EAT	Equatorial Atlantic
CAS	Central Asia	EPE	Equatorial Pacific East
CGI	Eastern Canada	EPW	Equatorial Pacific West
CNA	Central North America	HBO	Hudson Bay
EAF	East Africa	IND	Indian Ocean
EAS	East Asia	MED	Mediterranean Ocean
ENA	East North America	NAT	North Atlantic
NAS	Northern Asia	NNA	Far Northern Atlantic
NAU	North Australia	NNE	Far Northeastern Pacific
NEU	Northern Europe	NNW	Far Northwestern Pacific
SAF	Southern Africa	NPE	North Pacific East
SAH	Sahara	NPW	North Pacific West
SAS	South Asia	SAT	South Atlantic
SAU	South Australia	SIO	South Indian Ocean
SEA	Southeast Asia	SPE	South Pacific East
SEU	Mediterranean Land	SPW	South Pacific West
SSA	Southern South America	WPE	West Pacific East
TIB	Tibetan Plateau	WPN	West Pacific North
WAF	West Africa	WPS	WestPacific South
WNA	West North America		

LIST OF FIGURES

- Fig. 1.** Illustration of the effect of aggregation in time on precipitation distribution changes under CO₂-forced climate change, for an illustrative location in E. North America (108 x 108 km centered around Sharon Township, MI, 42.21°N, 84.04°W). Data shown is raw output from high-resolution (12 km) dynamically downscaled model runs (WRF driven by CCSM4), 10 years each of historical and future (RCP8.5) scenarios. Rows show 3 analysis methods – histograms, quantile-quantile plots, and quantile ratios – and columns show three time aggregations (3-hourly, daily, and monthly averages). In quantile ratio plots, the x axis is limited to the fraction of the distribution with nonzero precipitation (to avoid divide-by-zero errors). In q-q plots, some quantiles farther than 7 standard deviations from the mean are represented by crosses for clarity. A linear q-q plot with an intercept at 0 would imply that the future precipitation distribution equals the past distribution multiplied by a constant factor; this condition would produce a flat quantile ratio plot whose value is the slope. For comparison we show expected behavior if future precipitation followed scaling by 1) Clausius-Clapeyron (dashed blue) 2) the local mean intensity change (total precipitation in a timestep / length of timestep over which it occurs) (purple), 3) the local mean overall precipitation change (green), and 4) no change (dashed grey). At 3-hourly timescale, peak intensities rise as Clausius-Clapeyron, and the future precipitation distribution widens more than implied by a simple multiplicative shift (quantile ratio plot slopes upwards to the right). At daily timescale, both effects are moderated. At monthly timescale, the future precipitation distribution approaches a simple multiplicative shift by the fractional mean change. Behavior is robust to removing values with 0 precipitation (Figure S4) or considering only summer (Figure S2) or winter (Figure S3). 46
- Fig. 2.** Illustration showing that future changes in precipitation variability exceed those in precipitation means at fine resolution, but decrease with aggregation in either space or time. Figure shows fractional changes in deseasonalized precipitation over E. North America (see Figure 7 for regional boundaries) from the 3-hourly, 12 km dynamically downscaled WRF runs of Figure 1 (for comparison with raw, undeseasonalized data, see Figure S8). Precipitation changes are calculated for model output progressively aggregated over time (left) and space (right); we show the average change across the entire region. Model output in temporal aggregations at left are at 12 km spatial resolution; those in spatial aggregations at right are at 3 hourly temporal resolution. Means differ between panels because regions are defined slightly differently to simplify aggregation (see Figure S6). Edge effects produce slight changes in means for different aggregation levels. 47
- Fig. 3.** Distributions of regional annual average precipitation (removing seasonality, see Figure S13 for monthly results and Section S6 for other models) for CESM 1.0.4 preindustrial (blue) and future (red) runs using 500 years of data, for all land regions, ordered approximately geographically. Regions are those used in Castruccio et al. (2013); see Table A1 and Figure A1 for region codes and boundaries. Black dashed line shows a synthetic future distribution constructed by multiplying the preindustrial distribution by the fractional mean change (Equation 1). Blue and red dashed lines show the mean value of the present and future distributions, respectively. Future distributions generally resemble simple multiplication of past distributions, though often with a slight broadening beyond expectations based on the mean change. Many regions with the most evident broadening are geographically contiguous (e.g. W. and Central N. America and Central America; E., W., and S. Africa) and include a ‘drying’ region in which future mean precipitation declines (e.g. Central America, S. Africa). See Figure S11 for ocean regions and Table S1 for all mean and variability change values. 48
- Fig. 4.** Quantile ratio plots, showing the change in individual quantiles against cumulative probability for the annual CESM 1.0.4 precipitation of Figure 3 (see Section S6 for other models).

We compare model precipitation to two ‘synthetic’ distributions; the simple mean shift of Equation 1 (black dot-dashed), and the mean shift plus rescaling by an extra standard deviation change of Equation 2 (turquoise dashed). Panels are centered on the mean shift in black and y-axis ranges span an equal log distance in each figure. Y-axes are log-scaled, so that changes of e.g. 5/4 and 4/5 of the mean shift are the same distance from the gray center line. Where possible we show the no-change condition as a solid grey line at value 1. A positive slope implies a distribution broader than that produced by a simple mean change ($\epsilon_\sigma > 1$); a negative slope the opposite. (Note however that the magnitudes of slopes depend not only on the extra broadening ($1 - \epsilon_\sigma$), but also on the magnitude of the mean precipitation shift μ_f/μ_i and the shape of the distribution. For values see Tables S1 and S2.) Legends show p-values for an Anderson-Darling test between the model future distributions and those predicted by Equation 2. Higher p values imply less evidence that the two underlying distributions are different; by the typical cutoff for significance of $p=0.05$, all changes in annual data are consistent with Equation 2. Most future distributions show slight excess broadening over that expected from a mean shift alone, but the opposite holds in the high latitudes. Global land mean annual precipitation rises by 15% (green line in bottom right panel) while its variability rises by 20%, for an ϵ_σ of 1.05. 49

Fig. 5. Fractional changes in variability and means of monthly deseasonalized precipitation, shown as maps (a) and scatterplots (b), with change defined as the log ratio of future / pre-industrial control. We separately show variability changes at subannual and interannual frequencies. Maps (a) show one representative model from each of LongRunMIP and CMIP5 (CESM 1.0.4 and GFDL-CM3, respectively, with changes calculated from 500 and 30 year segments). Stippling indicates pixels without meaningful changes. (See Section 3e for uncertainty quantification). The longer LongRunMIP timeseries allow determining changes even at low frequencies. (Forcing is also higher in the $4\times\text{CO}_2$ LongRunMIP runs vs. the $\sim 3\times$ change in CMIP, and the LongRunMIP runs are fully stationary.) For interannual variability, LongRunMIP CESM shows significant changes over 87% of land area, vs. 20% in CMIP5 GFDL. Scatterplots (b) show all LongRunMIP and half of CMIP5 models. Mean changes are on the x axis and points are colored by the absolute value of latitude at each location. Solid line shows the orthogonal least squares fit (Section 3), conducted on all grid cells though we show only 1/5 (randomly chosen) here for clarity. Values beyond axis limits are plotted at the closest limit, and symbol size scales with area of each grid cell. Black dots mark the mean of changes across locations. If variabilities and means shifted equally, all points would fall on the 1:1 line (dashed). Points above the 1:1 line have a wider future distribution than expected from the mean shift ($\epsilon_\sigma > 1$), and those below a narrower one ($\epsilon_\sigma < 1$). Fitted slopes are generally < 1 , though interannual variability changes in CMIP5 are noisy and resulting slopes higher. Models with higher spatial resolution have more points shown and generally larger spreads – compare CCSM4 at ~ 140 km to CanESM2 and BCC-CSM1 at ~ 300 km – but fitted relationships explain similar fractions of variation. All tested models are similar. For analogous figures of remaining models, see Figures S16 (maps) and S17 (scatterplots), and see Table S3 for all fitted slopes, global $\bar{\epsilon}_\sigma$, and correlations. 50

Fig. 6. Characteristics of the relationship between mean and variability changes across all 12 CMIP5 and 6 LongRunMIP models examined. Slope (left) and area-weighted correlation (middle) of precipitation variability vs. mean change fits and ϵ_σ (right) are broken down by subannual and inter-annual frequencies. Data for all LongRunMIP models and 6 CMIP5 models are shown in Figure 5; for remaining models see Figure S17. Correlations are high and slopes for subannual variability are similar across models and consistently < 1 . For inter-annual variability, CMIP5 output is likely too short for realistic results, but all LongRunMIP models show $\beta < 1$. ϵ_σ is slightly above one for most models, consistent with prior published studies. 51

- Fig. 7.** Summary figure showing fractional changes in subannual precipitation variability vs. those in means for 6 LongRunMIP models (red) and 12 CMIP5 models (dark blue = monthly precipitation; light blue = daily). Figure shows area-weighted average changes across a region, normalized by the global or regional temperature change. Normalization does not qualitatively alter results since $\bar{\epsilon}_\sigma$ is not correlated with temperature change (Pearson’s correlation coefficient of -0.05, see Figure S24). Black dotted lines are fitted slopes through all grid cells in each region as in Figure 5b. See Figure S20 for an equivalent calculation based on the means of Figure 5b; conclusions are robust to the method chosen. Global means suggest an increase in variability greater than the increase in mean precipitation (top left), but the dependence on these mean changes implies that the behavior is regionally specific. At higher latitudes, where future precipitation increases strongly, variability changes are universally less than mean changes (bottom right). Much of the global signal of “extra broadening” results from the drying subtropics (bottom left). 52
- Fig. 8.** Evaluation of frequency dependence of precipitation variability changes. Figure shows fractional changes in interannual vs. subannual variability, expressed as the log ratio, as scatterplots (a) and maps (b). In scatterplots (a), subannual variability is on the x axis and points are colored by the absolute latitude at each location. Solid line shows the first principal component fit. Fits are conducted on all grid cells in each subset but we show only 1/5 here for clarity. Values beyond axis limits are plotted at the closest limit, and symbol size scales with area of each grid cell. Outside the tropics, changes in variability are effectively frequency-independent. Mean area-weighted correlation coefficient across models is 0.97 (range 0.95–0.98) and mean slope is 1.03 (range 0.99–1.10). Within the tropics, behavior is more diverse, and changes in interannual variability are generally lower than those in subannual variability in all but the MPI-ESM-12 model: for non-MPI models, 71% of tropical grid cells have lower interannual than subannual variability changes. The effect is localized in the Pacific and likely related to a dampened ENSO (Callahan et al. 2019), which is more evident in LongRunMIP models than in previous intercomparisons (Maher et al. 2018). 53
- Fig. A1.** Map of regions used in Figures 3, 4, S5-15, and Section S6 taken from Castruccio et al. (2013). Long names for each region are listed in Table 7. 54

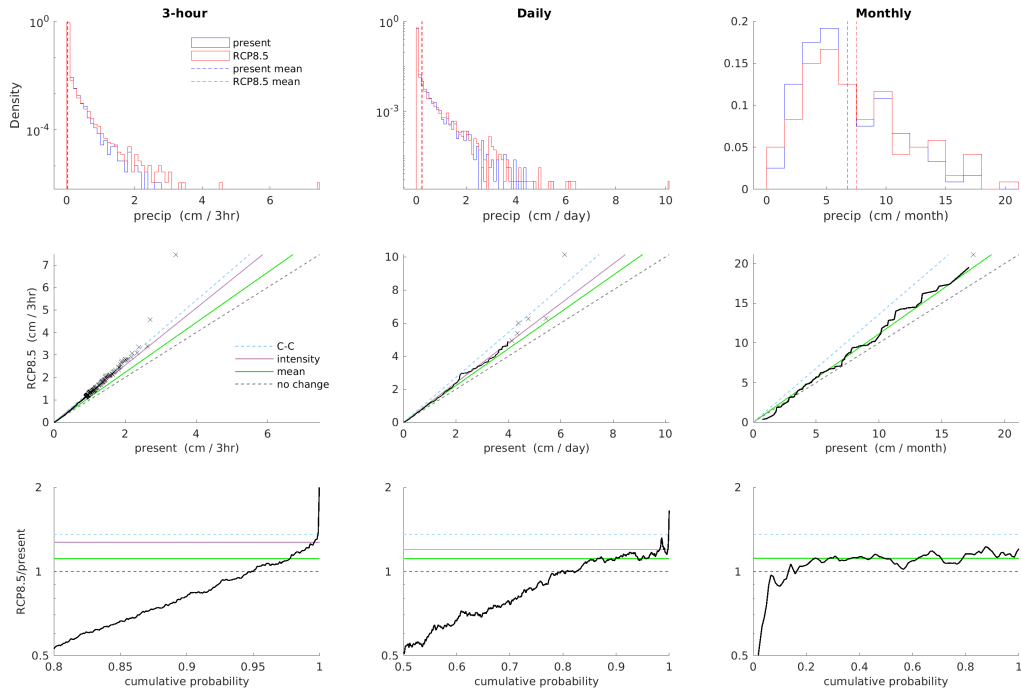


FIG. 1. Illustration of the effect of aggregation in time on precipitation distribution changes under CO₂-forced climate change, for an illustrative location in E. North America (108 x 108 km centered around Sharon Township, MI, 42.21°N, 84.04°W). Data shown is raw output from high-resolution (12 km) dynamically downscaled model runs (WRF driven by CCSM4), 10 years each of historical and future (RCP8.5) scenarios. Rows show 3 analysis methods – histograms, quantile-quantile plots, and quantile ratios - and columns show three time aggregations (3-hourly, daily, and monthly averages). In quantile ratio plots, the x axis is limited to the fraction of the distribution with nonzero precipitation (to avoid divide-by-zero errors). In q-q plots, some quantiles farther than 7 standard deviations from the mean are represented by crosses for clarity. A linear q-q plot with an intercept at 0 would imply that the future precipitation distribution equals the past distribution multiplied by a constant factor; this condition would produce a flat quantile ratio plot whose value is the slope. For comparison we show expected behavior if future precipitation followed scaling by 1) Clausius-Clapeyron (dashed blue) 2) the local mean intensity change (total precipitation in a timestep / length of timestep over which it occurs) (purple), 3) the local mean overall precipitation change (green), and 4) no change (dashed grey). At 3-hourly timescale, peak intensities rise as Clausius-Clapeyron, and the future precipitation distribution widens more than implied by a simple multiplicative shift (quantile ratio plot slopes upwards to the right). At daily timescale, both effects are moderated. At monthly timescale, the future precipitation distribution approaches a simple multiplicative shift by the fractional mean change. Behavior is robust to removing values with 0 precipitation (Figure S4) or considering only summer (Figure S2) or winter (Figure S3).

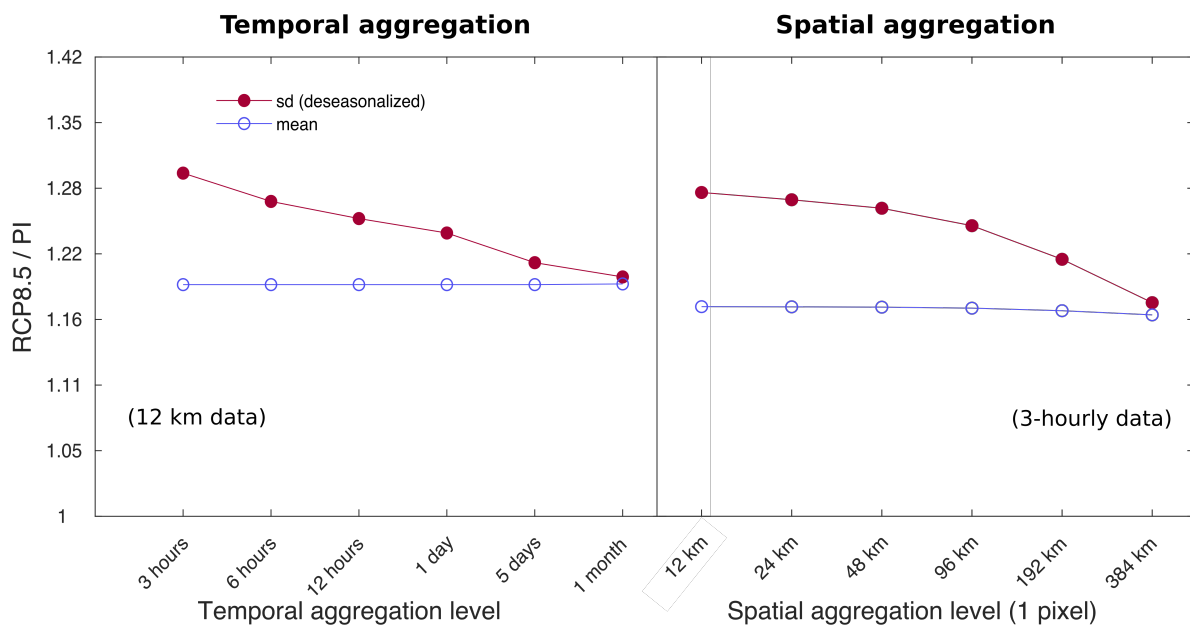


FIG. 2. Illustration showing that future changes in precipitation variability exceed those in precipitation means at fine resolution, but decrease with aggregation in either space or time. Figure shows fractional changes in deseasonalized precipitation over E. North America (see Figure 7 for regional boundaries) from the 3-hourly, 12 km dynamically downscaled WRF runs of Figure 1 (for comparison with raw, undeseasonalized data, see Figure S8). Precipitation changes are calculated for model output progressively aggregated over time (left) and space (right); we show the average change across the entire region. Model output in temporal aggregations at left are at 12 km spatial resolution; those in spatial aggregations at right are at 3 hourly temporal resolution. Means differ between panels because regions are defined slightly differently to simplify aggregation (see Figure S6). Edge effects produce slight changes in means for different aggregation levels.

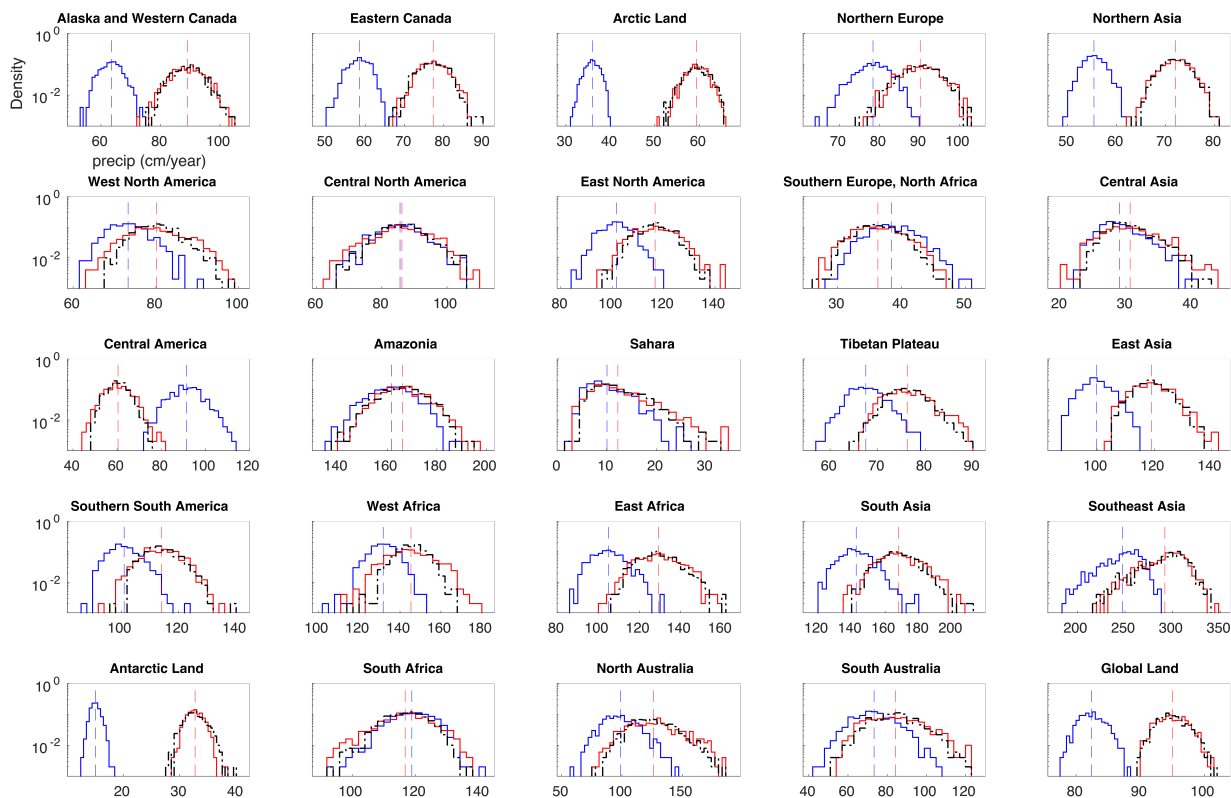


FIG. 3. Distributions of regional annual average precipitation (removing seasonality, see Figure S13 for monthly results and Section S6 for other models) for CESM 1.0.4 preindustrial (blue) and future (red) runs using 500 years of data, for all land regions, ordered approximately geographically. Regions are those used in Castruccio et al. (2013); see Table A1 and Figure A1 for region codes and boundaries. Black dashed line shows a synthetic future distribution constructed by multiplying the preindustrial distribution by the fractional mean change (Equation 1). Blue and red dashed lines show the mean value of the present and future distributions, respectively. Future distributions generally resemble simple multiplication of past distributions, though often with a slight broadening beyond expectations based on the mean change. Many regions with the most evident broadening are geographically contiguous (e.g. W. and Central N. America and Central America; E., W., and S. Africa) and include a ‘drying’ region in which future mean precipitation declines (e.g. Central America, S. Africa). See Figure S11 for ocean regions and Table S1 for all mean and variability change values.

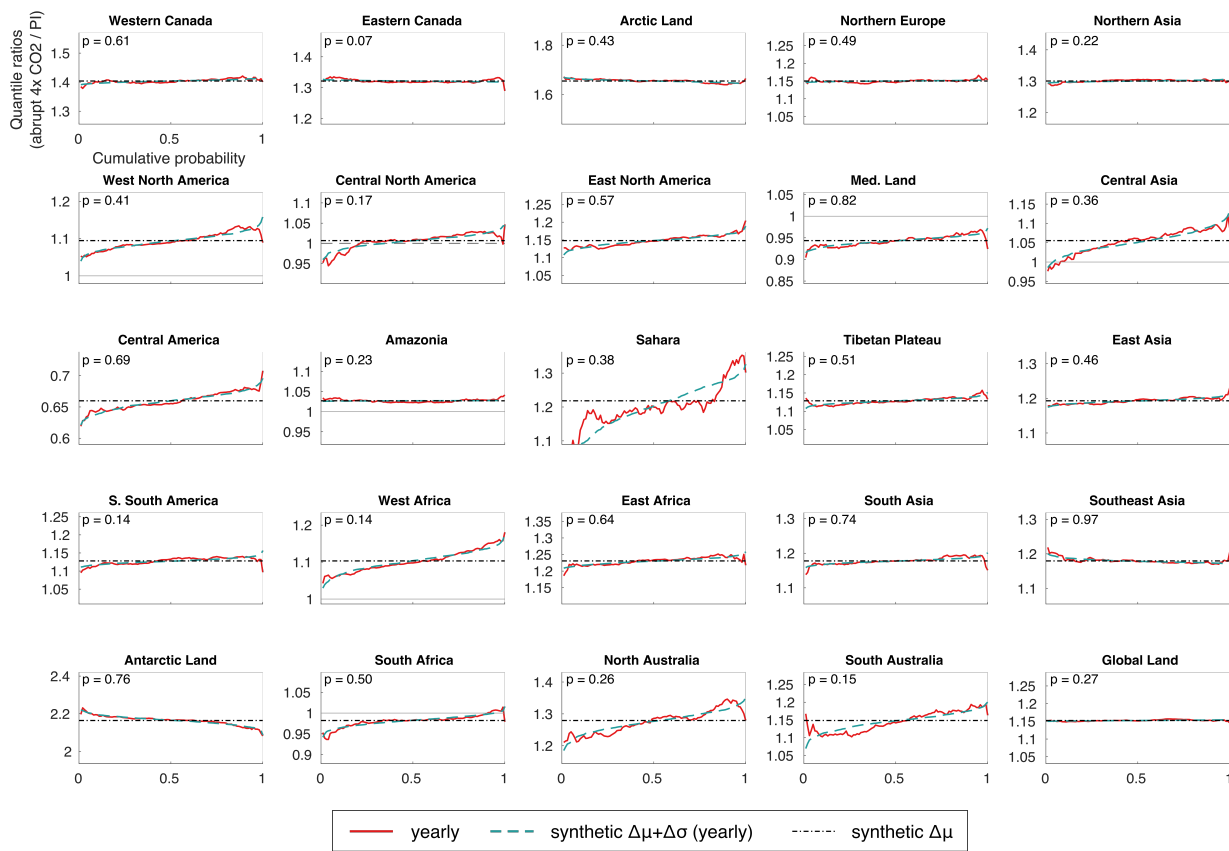


FIG. 4. Quantile ratio plots, showing the change in individual quantiles against cumulative probability for the annual CESM 1.0.4 precipitation of Figure 3 (see Section S6 for other models). We compare model precipitation to two ‘synthetic’ distributions; the simple mean shift of Equation 1 (black dot-dashed), and the mean shift plus rescaling by an extra standard deviation change of Equation 2 (turquoise dashed). Panels are centered on the mean shift in black and y-axis ranges span an equal log distance in each figure. Y-axes are log-scaled, so that changes of e.g. $5/4$ and $4/5$ of the mean shift are the same distance from the gray center line. Where possible we show the no-change condition as a solid grey line at value 1. A positive slope implies a distribution broader than that produced by a simple mean change ($\epsilon_\sigma > 1$); a negative slope the opposite. (Note however that the magnitudes of slopes depend not only on the extra broadening ($1 - \epsilon_\sigma$), but also on the magnitude of the mean precipitation shift μ_f/μ_i and the shape of the distribution. For values see Tables S1 and S2.) Legends show p-values for an Anderson-Darling test between the model future distributions and those predicted by Equation 2. Higher p values imply less evidence that the two underlying distributions are different; by the typical cutoff for significance of $p=0.05$, all changes in annual data are consistent with Equation 2. Most future distributions show slight excess broadening over that expected from a mean shift alone, but the opposite holds in the high latitudes. Global land mean annual precipitation rises by 15% (green line in bottom right panel) while its variability rises by 20%, for an ϵ_σ of 1.05.

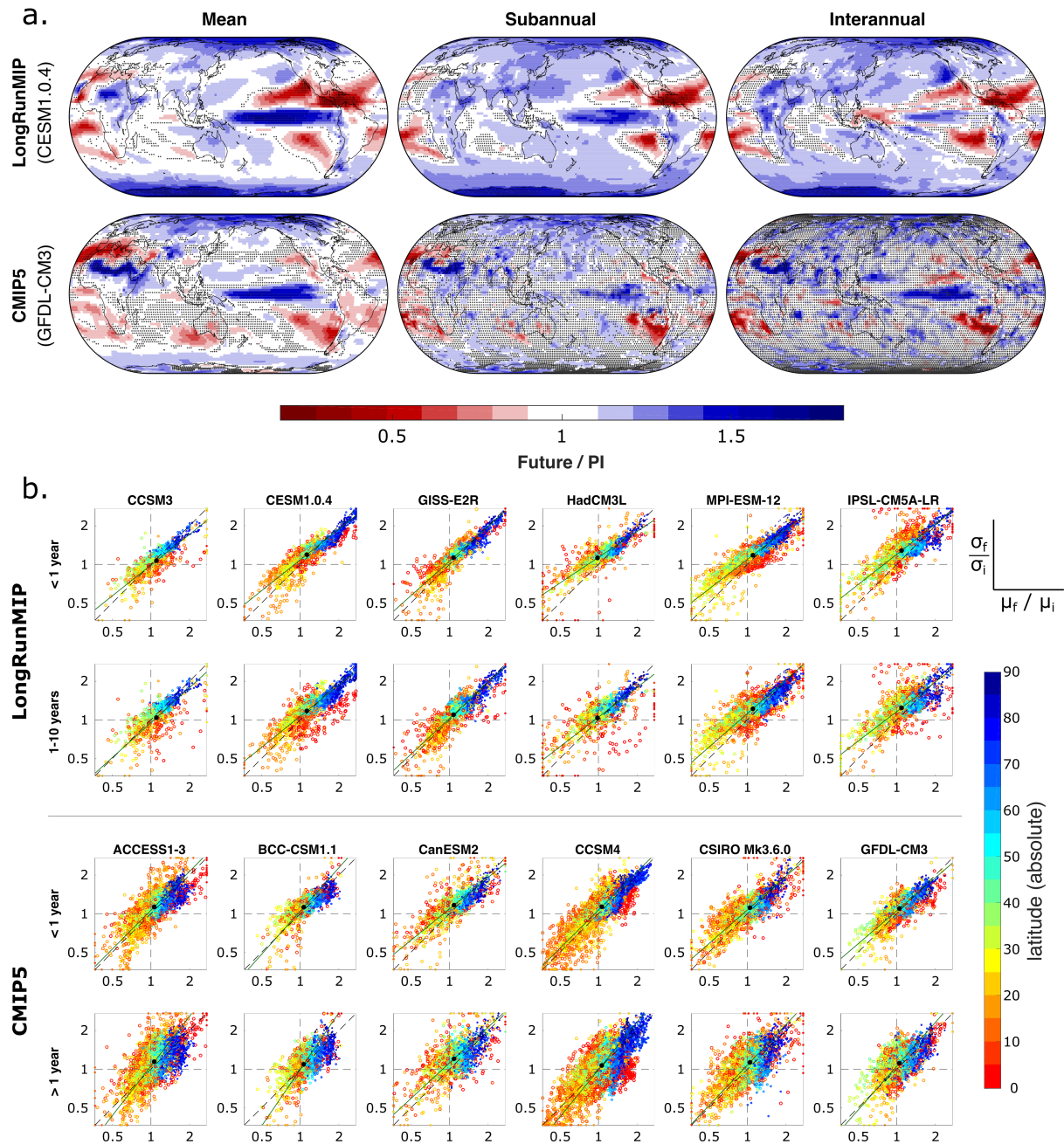


FIG. 5. Fractional changes in variability and means of monthly deseasonalized precipitation, shown as maps (a) and scatterplots (b), with change defined as the log ratio of future / pre-industrial control. We separately show variability changes at subannual and interannual frequencies. Maps (a) show one representative model from each of LongRunMIP and CMIP5 (CESM 1.0.4 and GFDL-CM3, respectively, with changes calculated from 500 and 30 year segments). Stippling indicates pixels without meaningful changes. (See Section 3e for uncertainty quantification). The longer LongRunMIP timeseries allow determining changes even at low frequencies. (Forcing is also higher in the $4\times\text{CO}_2$ LongRunMIP runs vs. the $\sim 3\times$ change in CMIP, and the LongRunMIP runs are fully stationary.) For interannual variability, LongRunMIP CESM shows significant changes over 87% of land area, vs. 20% in CMIP5 GFDL. Scatterplots (b) show all LongRunMIP and half of CMIP5 models. Mean changes are on the x axis and points are colored by the absolute value of latitude at each location. Solid line shows the orthogonal least squares fit (Section 3), conducted on all grid cells though we show

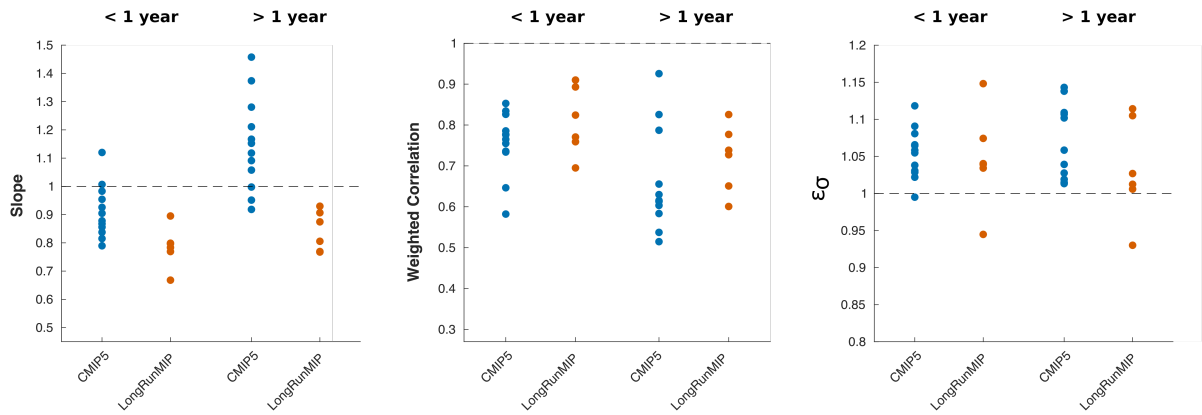


FIG. 6. Characteristics of the relationship between mean and variability changes across all 12 CMIP5 and 6 LongRunMIP models examined. Slope (left) and area-weighted correlation (middle) of precipitation variability vs. mean change fits and ε_{σ} (right) are broken down by subannual and inter-annual frequencies. Data for all LongRunMIP models and 6 CMIP5 models are shown in Figure 5; for remaining models see Figure S17. Correlations are high and slopes for subannual variability are similar across models and consistently < 1 . For inter-annual variability, CMIP5 output is likely too short for realistic results, but all LongRunMIP models show $\beta < 1$. ε_{σ} is slightly above one for most models, consistent with prior published studies.

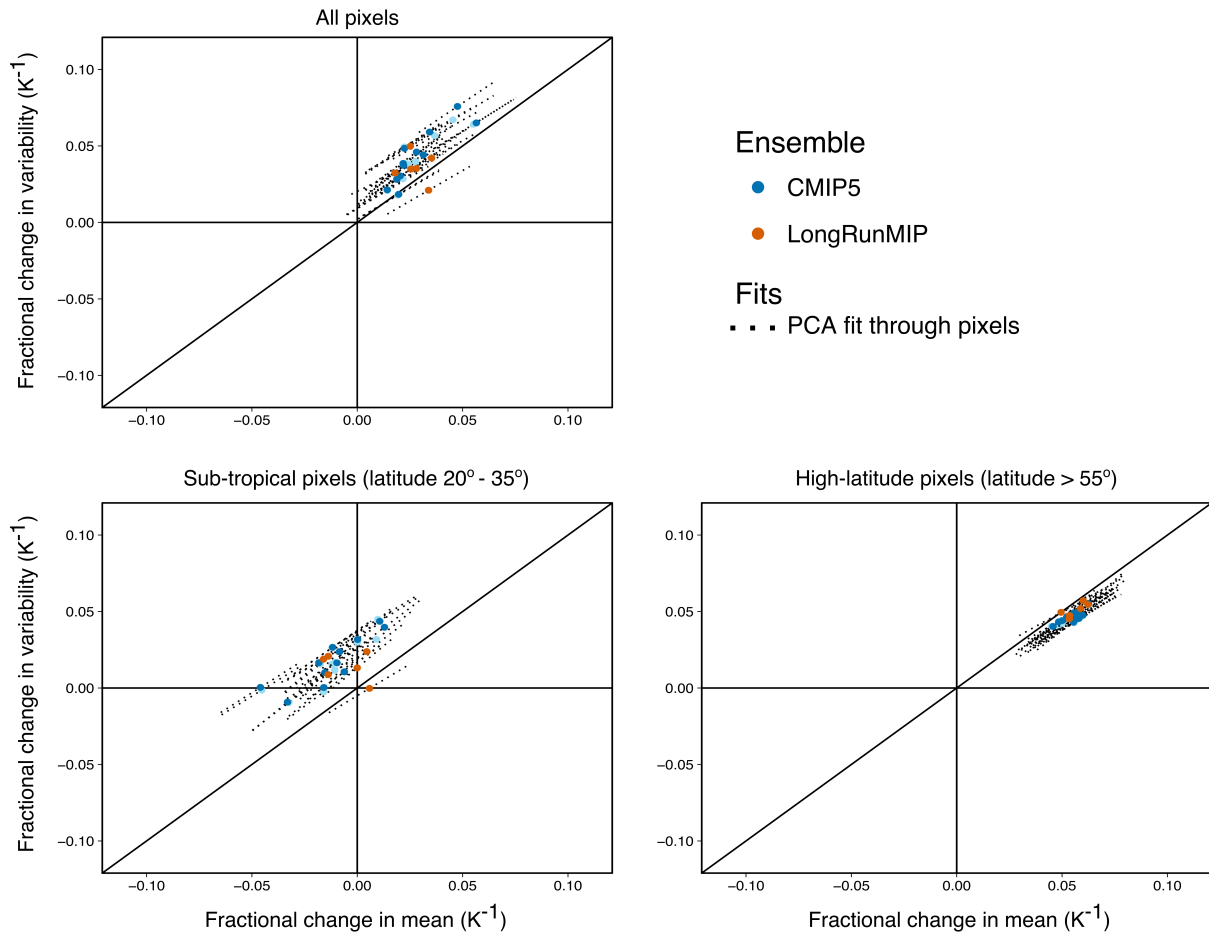


FIG. 7. Summary figure showing fractional changes in subannual precipitation variability vs. those in means for 6 LongRunMIP models (red) and 12 CMIP5 models (dark blue = monthly precipitation; light blue = daily). Figure shows area-weighted average changes across a region, normalized by the global or regional temperature change. Normalization does not qualitatively alter results since $\bar{\epsilon}_\sigma$ is not correlated with temperature change (Pearson's correlation coefficient of -0.05, see Figure S24). Black dotted lines are fitted slopes through all grid cells in each region as in Figure 5b. See Figure S20 for an equivalent calculation based on the means of Figure 5b; conclusions are robust to the method chosen. Global means suggest an increase in variability greater than the increase in mean precipitation (top left), but the dependence on these mean changes implies that the behavior is regionally specific. At higher latitudes, where future precipitation increases strongly, variability changes are universally less than mean changes (bottom right). Much of the global signal of “extra broadening” results from the drying subtropics (bottom left).

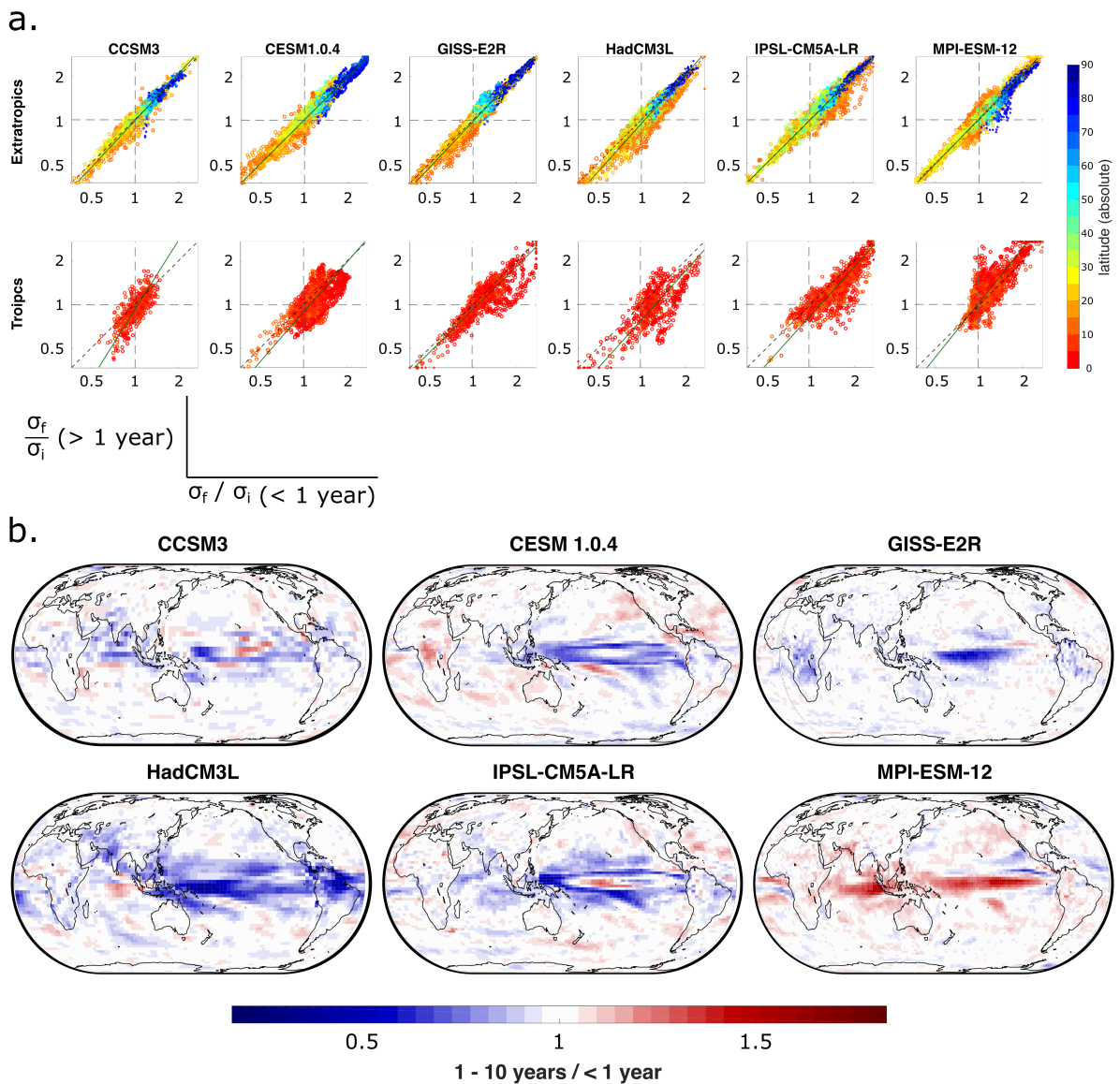


FIG. 8. Evaluation of frequency dependence of precipitation variability changes. Figure shows fractional changes in interannual vs. subannual variability, expressed as the log ratio, as scatterplots (a) and maps (b). In scatterplots (a), subannual variability is on the x axis and points are colored by the absolute latitude at each location. Solid line shows the first principal component fit. Fits are conducted on all grid cells in each subset but we show only 1/5 here for clarity. Values beyond axis limits are plotted at the closest limit, and symbol size scales with area of each grid cell. Outside the tropics, changes in variability are effectively frequency-independent. Mean area-weighted correlation coefficient across models is 0.97 (range 0.95–0.98) and mean slope is 1.03 (range 0.99–1.10). Within the tropics, behavior is more diverse, and changes in interannual variability are generally lower than those in subannual variability in all but the MPI-ESM-12 model: for non-MPI models, 71% of tropical grid cells have lower interannual than subannual variability changes. The effect is localized in the Pacific and likely related to a dampened ENSO (Callahan et al. 2019), which is more evident in LongRunMIP models than in previous intercomparisons (Maher et al. 2018).

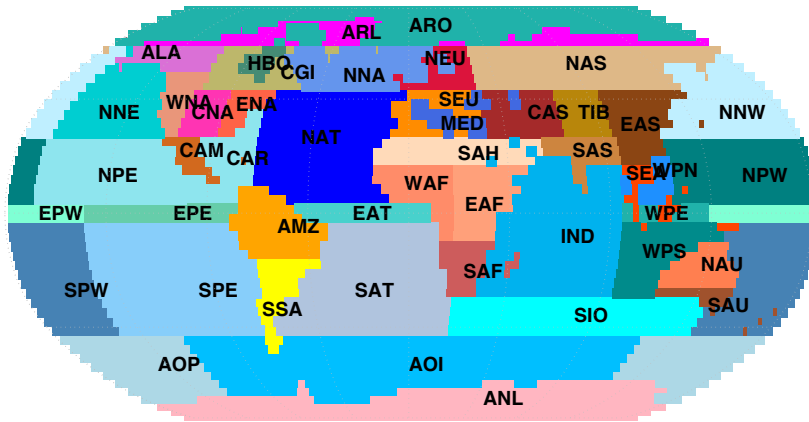


Fig. A1. Map of regions used in Figures 3, 4, S5-15, and Section S6 taken from Castruccio et al. (2013). Long names for each region are listed in Table 7.